

Visiting Scientist mission report


Document NWPSAF-KN-VS-013

Version 1.0

26 March 2013

Signatures of upscale and downscale energy transfer deduced from a third-order structure function analysis of scatterometer winds over the tropical Pacific

Gregory P. King, Jur Vogelzang and Ad Stoffelen

<p>The EUMETSAT Network of Satellite Application Facilities</p>		<p>Signatures of upscale and downscale energy transfer deduced from a third-order structure function analysis of scatterometer winds over the tropical Pacific</p>	<p>Doc ID : NWPSAF-KN-VS-013 Version : 1.0 Date : 26.3.13</p>
---	---	--	---

This documentation was developed within the context of the EUMETSAT Satellite Application Facility on Numerical Weather Prediction (NWP SAF), under the Cooperation Agreement dated 29 June 2011, between EUMETSAT and the Met Office, UK, by one or more partners within the NWP SAF. The partners in the NWP SAF are the Met Office, ECMWF, KNMI and Météo France.

Copyright 2013, EUMETSAT, All Rights Reserved.

Change record			
Version	Date	Author / changed by	Remarks
1.0	26.3.13	G.P.King, J.Vogelzang and A.Stoffelen	Final version for publication on NWP SAF website

Signatures of upscale and downscale energy transfer deduced from a third-order structure function analysis of scatterometer winds over the tropical Pacific

Gregory P. King^{1,2}, *Jur Vogelzang*³ and *Ad Stoffelen*³

¹Centro de Geofísica - IDL, Campo Grande, C8, University of Lisbon, 1749-016, Lisbon, Portugal

²Instituto Gulbenkian de Ciência, Apartado 14, 2781-901 Oeiras, Portugal

³KNMI Royal Netherlands Meteorological Institute, Postbus 201, 3730 AE De Bilt, The Netherlands

Abstract

We calculate third-order structure functions (third-order moments of longitudinal and transverse velocity increments δu_L and δu_T) using winds at the bottom of the marine boundary layer measured by satellite scatterometers. According to turbulence theory, the sign of the third-order structure function, or equivalently the sign of the skewness S , identifies the direction of energy transfer, with $S < 0$ implying downscale transfer and $S > 0$ an upscale transfer. Using along-track (approximately meridional) near-surface winds inferred from scatterometer measurements by SeaWinds-on-QuikSCAT and ASCAT-on-MetOp-A, one-dimensional structure functions and skewness S_a were calculated for both rainy and dry regions in the tropical Pacific. S_a was found to asymptote to an approximate constant value when the separation variable r exceeded 200 - 300 km. The time evolution of S_a was followed using its value at 300 km, denoted S_a^* . We found that S_a^* varied in sign and magnitude regionally and seasonally. Decomposing S_a^* into divergent (where velocity increments $\delta u_{La} > 0$) and convergent (where $\delta u_{La} < 0$) components, the variability was shown to be due to the changing relative strength of convergence and divergence within a region. Thus our main result may be expressed as follows: (i) that there is a downscale signature ($S_a^* < 0$) where and when surface convergence (i.e., deep convection) dominates, (ii) an upscale signature ($S_a^* > 0$) where and when surface divergence dominates, and (iii) seasonal variations of S_a^* are due to seasonal variations in the amount of surface convergence and divergence. The link with surface convergence and divergence challenges the usual picture of mesoscale turbulence as either a 2D or 3D energy cascade.

We also show figures of velocity increment PDFs $P(\delta u_{La})$ and $P(\delta u_{Ta})$ and suggest that these should be emphasized in future work. Furthermore, in order to help generate ideas and facilitate modeling efforts by the scientific community, we recommend that a web-based data-mining application be developed to enable users to request velocity increment PDFs for specified regions and periods of time.

Contents

1	Introduction	5
2	Physical context	6
3	Scatterometers and data	8
3.1	Data	9
3.2	Study areas and samples	10
4	Data Analysis	13
4.1	Definitions	13
4.1.1	Velocity increments	13
4.1.2	Second-order structure functions	13
4.1.3	Third-order structure functions	14
4.2	Application to scatterometer winds	15
5	Results	17
6	Discussion	26
6.1	Understanding the sign	26
6.2	Decomposition of the skewness	26
6.3	Decomposition of the turbulent kinetic energy	28
6.4	Diurnal effects	31
6.5	PDFs of velocity increments	31
7	Conclusions	40

List of Tables

1	Geographical limits and nomenclature for the regions shown in Fig. 3 . . .	11
---	--	----

List of Figures

1	SST field and superimposed ocean wind vectors for a typical January in the Tropical Pacific. Labels identify the Inter-Tropical and South Pacific Convergence Zones (ITCZ and SPCZ).	7
2	Latitude-time plots of monthly and zonally averaged SST measured by the TRMM Microwave Imager (TMI) during the study period.	7
3	The boundaries of the nine geographical regions used in the present study. Nomenclature of the regions and their geographical limits are given in Table 1.	10
4	Latitude-time plots of monthly and zonally averaged rain-rate measured by the TRMM Microwave Imager (TMI) during the study period.	12
5	Monthly SRAD rain-rates for QuikSCAT morning and evening passes.	12
6	Structure function slope β estimated from fits to $\log D_{2a}$ vs. $\log r$ over the range 50-250 km. Error bars show the root-mean square deviation.	19
7	D_{3a} vs r (January 2009).	20
8	D_{3a} vs separation r . August 2009 — all regions. The line types and colors are the same as in Fig. 7.	21
9	Skewness vs separation r . January 2009 — all regions. The line types and colors are the same as in Fig. 7.	22
10	Skewness vs separation r . August 2009 — all regions. The line types and colors are the same as in Fig. 7.	23
11	Time series of S_a^* (skewness at 300 km). All wind products are shown. The line types and colors are the same as in Fig. 7. The bar graph shows monthly SRAD rain-rates (see black curve in Fig. 5).	24
12	As in Fig. 13, but comparison of NWP models winds with the 12.5 km products.	25
13	Time series S_a^* separated into divergent (Δ) and convergent (∇) contributions: QSCAT-12.5 (red) and NCEP-12.5 (black dashed).	27
14	Decomposition of K_{La} into divergent (Δ) and convergent (dashed line) contributions for ASCAT-12.5 (black) and QSCAT-12.5 (red).	29
15	Decomposition of K_{Ta} into cyclonic (\Leftarrow) and anti-cyclonic (dashed) contributions for ASCAT-12.5 (black) and QSCAT-12.5 (red).	30
16	Comparison of D_{3a} for the morning and evening passes in WPE January. Note that the QuikSCAT satellite crosses the equator at 06:30 and 18:30, while MetOp-A crosses three hours later at 09:30 and 21:30. The line types and colors are the same as in Fig. 7.	31

17	Regional variation of $P(\delta u_{La}^*)$, the longitudinal velocity increment PDF at $r = 300$ km, for January 2009: QSCAT-12.5 (—×—) ; NCEP-12.5 (—□—).	32
18	Regional variation of $P(\delta u_{La}^*)$, the longitudinal velocity increment PDF at $r = 300$ km, for August 2009: QSCAT-12.5 (—×—) ; NCEP-12.5 (—□—).	33
19	Time evolution of $P(\delta u_{La}^*)$ for the WPS: QSCAT-12.5 (—×—) ; NCEP-12.5 (—□—).	34
20	Time evolution of $P(\delta u_{La}^*)$ for the EPE: QSCAT-12.5 (—×—) ; NCEP-12.5 (—□—).	35
21	Regional variation of $P(\delta u_{Ta}^*)$, the transverse velocity increment PDF at $r = 300$ km, for January 2009: QSCAT-12.5 (—×—) ; NCEP-12.5 (—□—).	36
22	Regional variation of $P(\delta u_{Ta}^*)$, the transverse velocity increment PDF at $r = 300$ km, for August 2009: QSCAT-12.5 (—×—) ; NCEP-12.5 (—□—).	37
23	Time evolution of $P(\delta u_{Ta}^*)$ for the WPS: (—×—) QSCAT-12.5; (—□—) NCEP-12.5.	38
24	Time evolution of $P(\delta u_{Ta}^*)$ for the EPE.	39

1 Introduction

This paper is the last in a series of three on structure function analysis of ASCAT-on-MetOp-A and SeaWinds-on-QuikSCAT scatterometer-measured winds over the tropical Pacific. The two earlier papers calculated and compared spectra and second-order structure functions ([King et al., 2012, 2013](#)). Here we compare third-order structure functions.

This paper addresses a long-standing question in atmospheric dynamics: Is horizontal kinetic energy transferred to small scales through a downscale cascade as in ideal three-dimensional (3D) turbulence? Or is it transferred to large scales via a two-dimensional (2D) inverse cascade? The classic papers by [Nastrom et al. \(1984\)](#) and [Nastrom and Gage \(1985\)](#) and more recent papers by [Lindborg \(1999\)](#) and [Cho and Lindborg \(2001\)](#) have addressed this question through an analysis of global datasets of winds near the tropopause measured by instruments carried on commercial aircraft. Here we use winds at the bottom of the marine boundary layer inferred from radar backscatter from the ocean surface measured by ASCAT and SeaWinds.

[Nastrom et al. \(1984\)](#) calculated horizontal wind spectra and demonstrated that they follow a k^{-3} power law at large scales ($r > 1000$ km) and transition to a $k^{-5/3}$ power law at small scales ($2 < r < 300$ km). The k^{-3} range is consistent with Charney's theory of quasigeostrophic turbulence ([Charney, 1971](#)). The origin of the $k^{-5/3}$ range, however, continues to be debated. Two types of theories have been put forth: One is based on internal gravity wave dynamics ([Dewan, 1979](#); [Van Zandt, 1982](#); [Dewan, 1997](#)), which predicts a downscale cascade of energy from longer to shorter waves. The other is based on 2D and geostrophic turbulence ([Gage, 1979](#); [Lilly, 1983](#)). The basic picture is that geophysical constraints (stratification, rotation, thin atmosphere) decouple atmospheric motions into layers and energy sources at large-scale (e.g., baroclinic instability) and small-scale (e.g., convection and shearing instabilities) give rise to a combined energy and enstrophy inertial range that yields a $k^{-5/3}$ range at small-scales and a k^{-3} range at large-scales ([Lilly, 1989](#)). This 2D-like or stratified turbulence scenario implies an upscale energy cascade.

Scatterometer wind spectra are similar to the upper level spectra over the large meso-scale and transition regions. [Freilich and Chelton \(1986\)](#); [Wikle et al. \(1999\)](#); [Patoux and Brown \(2001\)](#); [Xu et al. \(2011\)](#) found power laws (for scales down to 200 km) varying between $k^{-1.9}$ and $k^{-2.9}$, with the shallowest spectra in the tropical Pacific and Atlantic, becoming steeper towards the poles, but with the steepest in the tropical Indian Ocean. Due to noise and processing issues, accurate power laws for scales below 200 km remain a challenge [Rodriguez and Chau \(2011\)](#); [King et al. \(2013\)](#). [Wikle et al. \(1999\)](#) expanded their analysis to smaller scales using high-resolution retrievals of 10-m winds from Doppler radar measurements from research aircraft. Their results were obtained using observations covering a domain in the tropical western Pacific during austral summer during the Tropical Ocean Global Atmosphere Coupled Ocean–Atmosphere Response Experiment (TOGA COARE) intensive observation period (IOP). For the combined spectra, they found a $k^{-5/3}$ power law down to 1 km. The $k^{-5/3}$ power law was noted to be consistent with an upscale energy cascade driven by an energy source at high wavenumbers thought to be associated with organized tropical convection.

The inability of the energy spectrum to distinguish between different theories led Lindborg ([Lindborg, 1999](#)) to develop a test based on the Kolmogorov third-order velocity structure function law [Kolmogorov \(1941\)](#). This law is more fundamental than the Kolmogorov $k^{-5/3}$ law ([Frisch, 1995](#); [Lindborg, 1996](#)). [Lindborg \(1999\)](#) reworked the Kolmogorov analysis to derive theoretical relationships for ideal (i.e., homogeneous, isotropic and non-divergent) 2D turbulence. He then argued that the sign of the third-order structure function $D_3(r)$ indicates the direction of the cascade: $D_3 < 0$ implies downscale and $D_3 > 0$ implies upscale. [Cho and Lindborg \(2001\)](#) found that D_3 was consistent with a downscale energy cascade in the small to intermediate scales, and an upscale energy cascade at the largest scales. Although their results argued against the stratified-upscale theory, in a later paper [Lindborg \(2007\)](#) argued against a gravity-wave mechanism and for a stratified-downscale scenario: that the layers created in stratified turbulence might go unstable to a shear instability, breaking the layer up into smaller structures, and hence a downscale cascade.

In this paper we apply the Lindborg third-order structure function test to several different QuikSCAT and ASCAT wind products. This paper is the third in a series of papers: the first two ([King et al., 2012, 2013](#)). In on second-order structure function analysis of scatterometer winds: who calculated second-order structure functions for rainy and dry regions in the tropical Pacific. The effects of both noise and spatial filtering and their variability as a function of wind product could be seen in the second-order structure functions. The differences were such that one might expect a third-order analysis to be troublesome. However, we will show that this is not the case. Instead the third-order results, expressed in terms of the skewness, show very good agreement across wind product. Our results also demonstrate that the sign of the third-order structure function varies regionally and seasonally, implying that the question in the first paragraph should not be phrased as 'either-or', but as 'where, when and why'.

The paper is structured as follows. Section 2 gives an overview of the tropical Pacific within which our study regions are defined. In section 3 the scatterometers, wind products, and study area are described. In section 4 velocity increments and structure functions are defined. The results of this paper are given in section 5 and discussed in section 6. In section we give our 7 and a recommendation that, following recent trends in the turbulence literature, that the full probability distribution of velocity increments be studied.

2 Physical context

Figure 1 shows sea surface temperatures (SST) for a typical August in the tropical Pacific between latitudes 30°S and 30°N; ocean wind vectors are superimposed on the SST in the figure. The convergence zones labeled in the figure play a central role in the organization of tropical circulations and generation of tropical weather systems. They are the InterTropical Convergence Zone (ITCZ), the western North Pacific Monsoon Trough (MT), the South Pacific Convergence Zone (SPCZ), and the East Pacific Warm Pool (EPWP). Also shown (Figure 2) are latitude-time plots of the monthly averaged SST over the period November 2008 - October 2009 in each longitudinal zone of the study area (see Fig. 3).

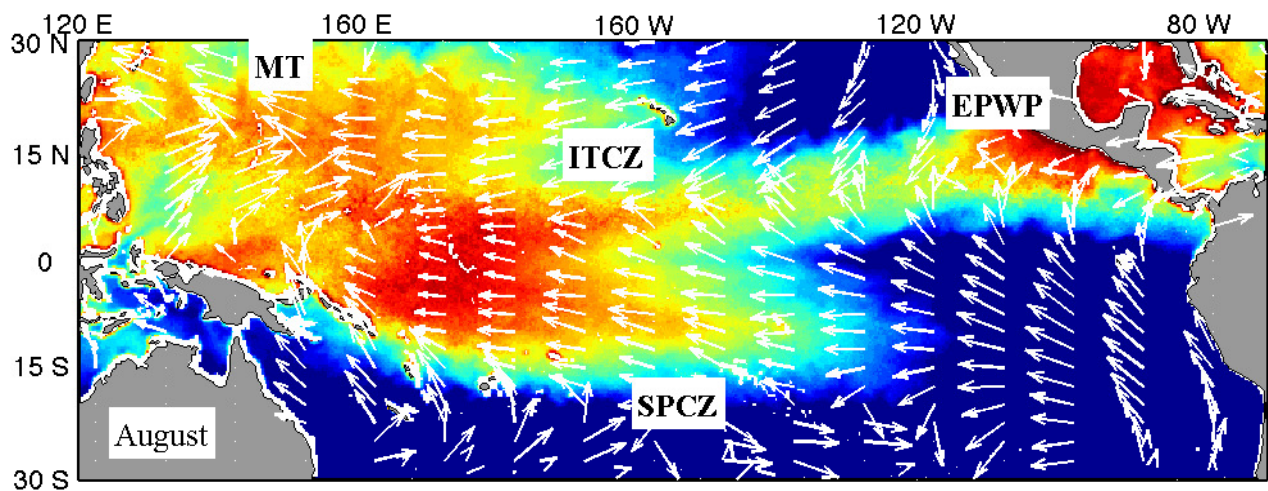


Fig. 1: SST field and superimposed ocean wind vectors for a typical January in the Tropical Pacific. Labels identify the Inter-Tropical and South Pacific Convergence Zones (ITCZ and SPCZ).

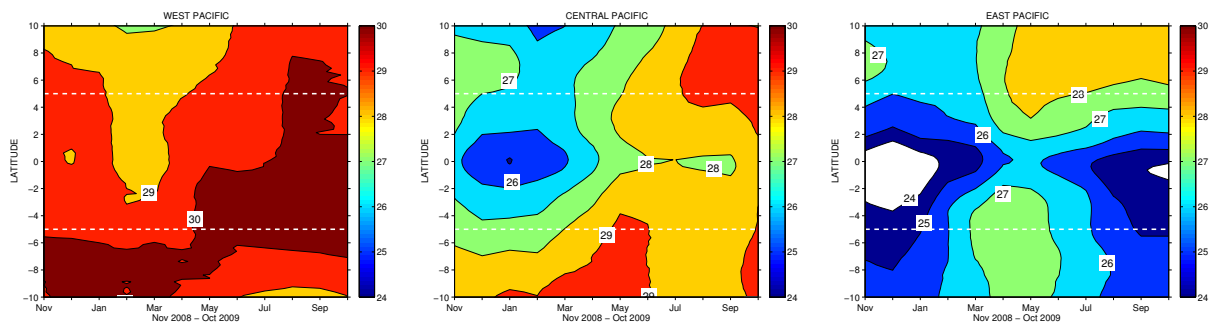


Fig. 2: Latitude-time plots of monthly and zonally averaged SST measured by the TRMM Microwave Imager (TMI) during the study period.

The ITCZ extends across the Pacific but in the east Pacific remains north of 4°N throughout the year. As boreal summer progresses, the ITCZ migrates north, merging with the EPWP in the eastern Pacific and with the MT in the western Pacific. The axis of the MT usually emerges from east Asia in boreal summer at about 20°- 25° N and extends south-eastward to a terminus southeast of Guam at (13° N, 145° E). Its oceanic portion shows considerable variability in position, shape, and orientation throughout the monsoon season (June-November) ([Lander, 1996](#)). The area near the trough axis is a favorable region for the genesis of tropical cyclones and monsoon depressions.

As boreal summer wanes, the ITCZ migrates southward and across the equator to merge with the SPCZ. As the ITCZ migrates southward, so too does the west Pacific warm pool, defined as the waters enclosed by the 28°C isotherm ([Wyrтки, 1989](#)), an empirical threshold for the onset of deep convection (see Fig. 2). The warm pool spans the western areas of the equatorial Pacific to the eastern Indian Ocean. The high SST in the warm pool creates an environment favorable to the self-organization of individual convection cells into Mesoscale Convective Systems (MCSs) with scales ~ 300 -400 km (c.f., [Houze, 2004](#)). These can self-organize into superclusters (~ 1000 -3000 km), which can in turn organize into a large-scale envelope known as the Madden-Julian Oscillation ($\sim 10,000$

km).

The SPCZ is present all year, starting parallel to the equator in the western Pacific before changing direction southeastwards across the Pacific. Convective activity in the SPCZ is greatest during austral summer, so that from November to April frequent and strong convective activity occurs near and just south of the equator. During boreal spring the area of strongest convergence rapidly moves across the equator and concentrates near the confluence of the ITCZ and MT (10°- 20° N) from May to October (see figure 1 in [Zhu and Wang, 1993](#)).

The southern boundary of the ITCZ in the east Pacific marks the location of a strong SST front that forms the northern boundary of a tongue of cool SST — the east Pacific *cold tongue*. The southern boundary of the cold tongue is formed by another strong SST front. The intensity and spatial extent of the cold tongue varies seasonally ([Mitchell and Wallace, 1992](#)). During the *warm season* (January-June), the ITCZ is nearest the equator and the cold tongue falls to minimum intensity and spatial extent. During the *wet season* (typically March-April) deep convection and rain enter the region. During the *cold season* (July-December), the ITCZ is furthest north and the cold tongue expands, reaching maximum intensity and spatial extent in August-September.

Not shown is another convergence zone that emerges south of the equator in the east Pacific from March to April ([Masunaga and L'Ecuyer, 2010](#), and references therein). This Southern ITCZ is caused by the deceleration of southerly surface winds as they pass over the SST front on the southern boundary of the cold tongue ([Liu and Xie, 2002](#)).

3 Scatterometers and data

The QuikSCAT satellite was launched by the National Aeronautics and Space Administration (NASA) in June 1999. The mission produced ocean vector winds from July 1999 until November 2009. The MetOp-A satellite was launched in October 2006 and is operated by the European Organisation for the Exploitation of Meteorological Satellites (EUMETSAT). Both satellites are in quasi-sun-synchronous orbits with an inclination angle of $\Theta = 98.6^\circ$. QuikSCAT crosses the equator at about 06:30 (ascending pass) and 18:30 (descending pass), while MetOp-A crosses the equator at about 09:30 (descending pass) and 21:30 (ascending pass).

The SeaWinds-on-QuikSCAT scatterometer is a rotating pencil-beam design with an 1800 km wide swath and transmits at Ku-band (13.4 GHz) ([Tsai et al., 2000](#)). The pencil-beam design has a complicated observation geometry that varies across the swath. This results in a varying performance that is poor in the nadir region and far swath. The ASCAT-on-MetOp-A scatterometer uses a dual-swath fan-beam configuration with two 550 km wide swaths separated by a nadir gap of about 700 km and transmits at C-band (5.3 GHz) ([Figa-Saldaña et al., 2002](#)). The fan-beam configuration has consistent measurement geometry and instrument performance.

3.1 Data

The radar backscatter detected by the scatterometers goes through two levels of processing to produce wind speed and wind direction. Level 1 processing involves averaging individual backscatter measurements and produces them on a regularly spaced grid. Level-2 takes the Level-1 data and applies quality control, an inversion step, and an ambiguity removal step. The inversion step applies an empirically derived geophysical model function (GMF) to relate backscatter (as a function of the wind direction) with the equivalent neutral-stability vector wind at a height of 10 meters. Due to the nature of radar backscatter from the ocean surface, this procedure usually provides multiple solutions referred to as ambiguities. An ambiguity removal algorithm is applied to produce the selected winds.

The wind products used in this paper are the same as used in [King et al. \(2013\)](#). A brief description follows.

ASCAT-12.5 and ASCAT-25 were produced to Level-1 by EUMETSAT. Level-1 cross-section data are calculated by averaging individual backscatter measurements. The weighting function chosen for this averaging is a two-dimensional Hamming window, designed to provide noise reduction and spatial resolution. Level-2 processing is carried out at the Royal Netherlands Meteorological Institute (KNMI) using the ASCAT Wind Data Processor (AWDP). The GMF used in the AWDP is CMOD5.n and ambiguity removal is carried out using a two-dimensional variational method (2DVAR) ([Vogelzang et al., 2009](#)).

SeaWinds-NOAA is a near-real-time product that was issued by the National Oceanic and Atmospheric Administration (NOAA) and is described in detail by [Hoffman and Leidner \(2005\)](#). Level-1B processing uses a centroid binning method that assigns a backscatter slice to only one WVC. The GMF is QSCAT-1 and ambiguity removal is carried out using a median filter (MF) followed by a sophisticated algorithm called Direction Interval Retrieval with Thresholded Nudging (DIRTH) ([Stiles et al., 2002](#)) — collectively referred to as MF+DIRTH.

SeaWinds-KNMI is a reprocessing of SeaWinds-NOAA by KNMI using improved (rain) quality control ([Portabella and Stoffelen, 2002](#)). The GMF is NSCAT-2, and ambiguity removal is carried out using 2DVAR and additional noise reduction by the Multiple Solution Scheme (MSS) ([Vogelzang et al., 2009](#)).

QSCAT-12.5 (version 3) is the recently released science data product produced by the NASA Jet Propulsion Laboratory (JPL). It is the result of a reprocessing of the entire SeaWinds on QuikSCAT mission with many algorithm improvements ([Fore et al., 2012](#)). Level-1B processing uses an overlap binning method that increases the number of backscatter slices being assigned to the same WVC. The GMF is Ku2011 and ambiguity removal is carried out using MF+DIRTH.

Collocated NWP forecasts interpolated to the swath grid are packaged with each product. The SeaWinds-NOAA and QSCAT products are collocated with NWP forecasts from the National Center for Environmental Prediction (NCEP) model. The ASCAT and

SeaWinds-KNMI products are collocated with NWP forecasts from the European Centre for Medium range Weather Forecasting (ECMWF) model. Only the winds packaged with the 12.5 km products are presented in this paper.

Rain affects the radar backscatter measured by scatterometers: the higher the radar frequency, the larger the impact of rain attenuation and scattering. As a result, rain is a larger source of error for winds derived from Ku-band instruments (SeaWinds) than from C-band instruments (ASCAT). For example, as many as 16% of wind retrievals from SeaWinds measurements over the west Pacific warm pool are flagged as rain-contaminated. In contrast, the lower ASCAT radar frequency results in winds that are much less affected by rain, although they are sensitive to secondary effects, such as the splashing of rain drops on the surface and local wind variability when rain is heavy. These secondary effects of rain are a source of ‘geophysical noise’, which at present are not flagged by quality control (*Portabella et al., 2012*).

Rain-rates were obtained from the Tropical Rainfall Measuring Mission’s (TRMM) Microwave Imager (TMI) on board the TRMM satellite. The TMI data were obtained from the Remote Sensing Systems Web site (<http://www.ssmi.com>). We also use SeaWinds Radiometer (SRAD) rain-rates. These are derived from SeaWinds measurements of the ocean radiometric brightness temperature (*Laupattarakasem et al., 2005*) and are included with the QuikSCAT 25 km L2B science data product (available from the Physical Oceanography Distributed Data Archive (PO.DAAC)).

3.2 Study areas and samples

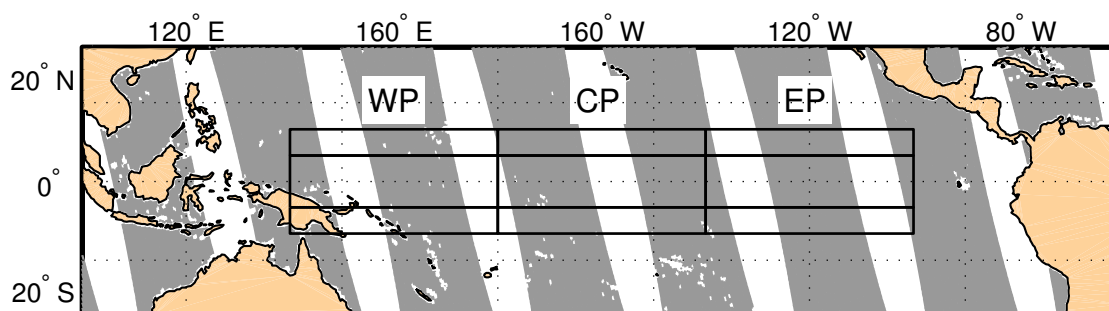


Fig. 3: The boundaries of the nine geographical regions used in the present study. Nomenclature of the regions and their geographical limits are given in Table 1.

Figure 3 shows the tropical Pacific subdivided into nine regions; some SeaWinds ascending swaths are shown shaded in grey. The latitude and longitude limits of the regions and their nomenclature are given in Table 1. The latitude-longitude limits were chosen to facilitate a comparison of structure functions in rainy and dry regions. The seasonal and regional variation in rain is illustrated in Figs. 4 and 5.

Samples were selected along-swath: WVCs in the same sample all have the same cross-swath index. Samples were checked and any wind vectors with coordinates outside the region of interest or that did not pass quality control were flagged as missing. In the case of SeaWinds-NOAA and QSCAT-12.5 wind vectors, wind vectors were flagged missing if

Tab. 1: Geographical limits and nomenclature for the regions shown in Fig. 3.

	<i>West Pacific</i> 140° – 180°E	<i>Central Pacific</i> 180° – 220°E	<i>East Pacific</i> 220° – 260°E
<i>North</i> 5° – 10°N	WPN (Rainy)	CPN (Rainy)	EPN (Rainy)
<i>Equator</i> 5°S – 5°N	WPE (Rainy)	CPE (Dry)	EPE (Dry)
<i>South</i> 10° – 5°S	WPS (Rainy)	CPS (Dry)	EPS (Dry)

the rain flag was set. In the case of ASCAT winds, wind vectors were flagged missing if the KNMI quality control flag or the variational quality control flag was set (see [KNMI, 2011](#), section 6.2). Samples from both the ascending and descending passes of the satellite and from the whole swath (including the outer and nadir parts of the SeaWinds swath) were used to calculate the structure functions.

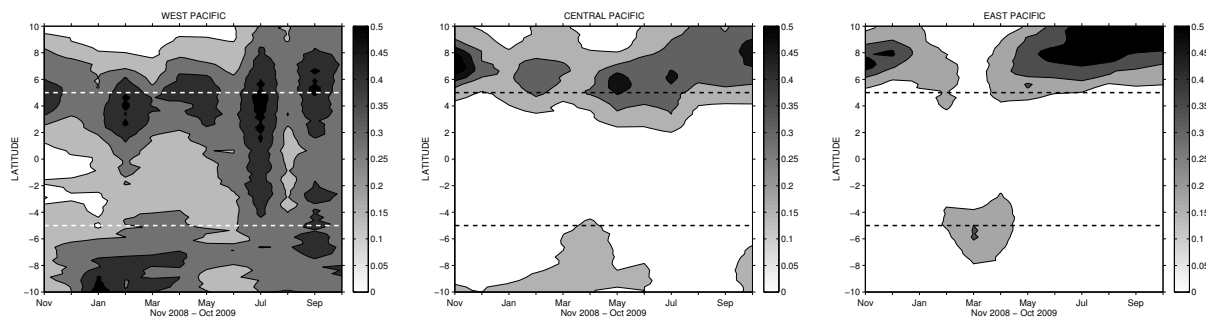


Fig. 4: Latitude-time plots of monthly and zonally averaged rain-rate measured by the TRMM Microwave Imager (TMI) during the study period.

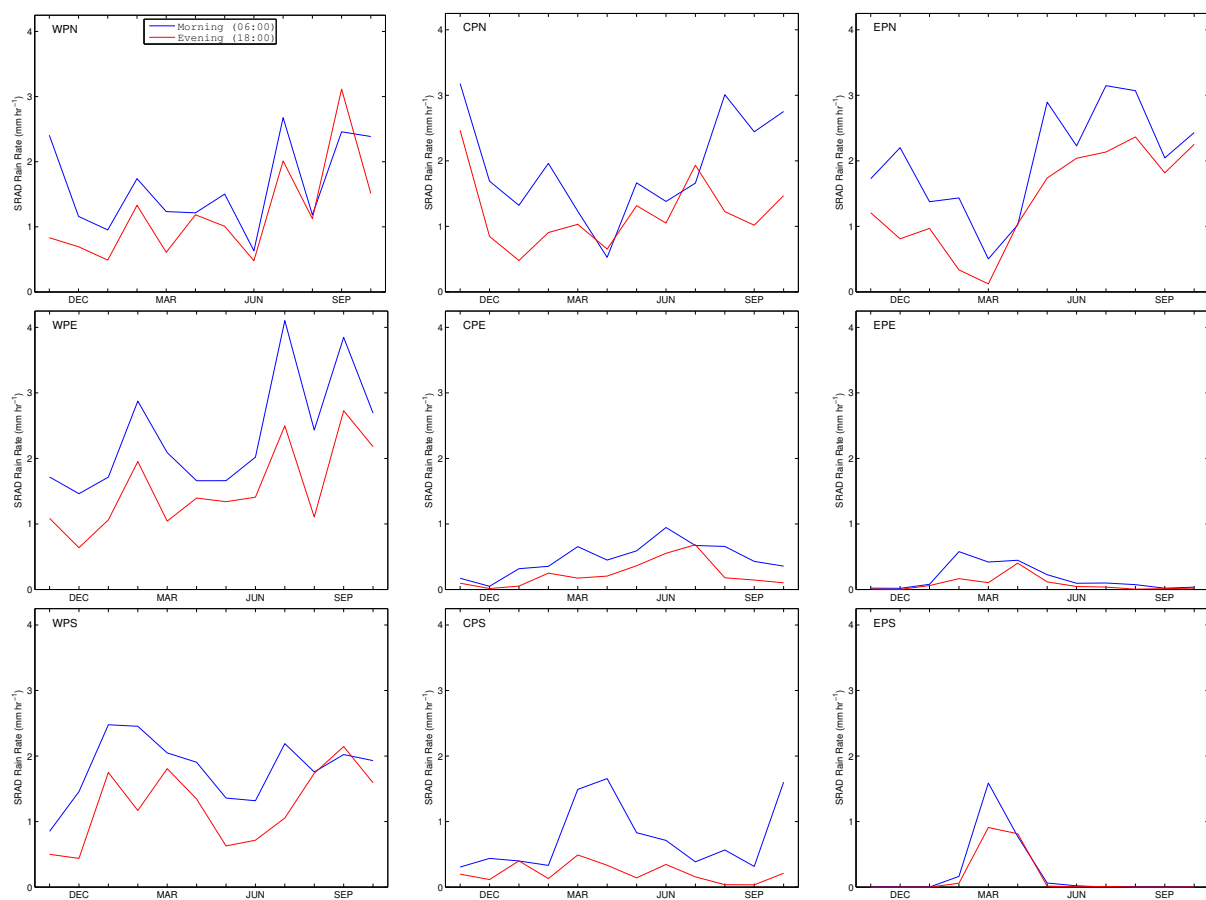


Fig. 5: Monthly SRAD rain-rates for QuikSCAT morning and evening passes.

4 Data Analysis

4.1 Definitions

4.1.1 Velocity increments

Turbulence theory focuses attention on velocity increments, the difference in velocity between two points \mathbf{x} and $\mathbf{x} + \mathbf{r}$

$$\begin{aligned}\delta u_L(\mathbf{x}, \mathbf{r}) &= u_L(\mathbf{x} + \mathbf{r}) - u_L(\mathbf{x}) \\ \delta u_T(\mathbf{x}, \mathbf{r}) &= u_T(\mathbf{x} + \mathbf{r}) - u_T(\mathbf{x})\end{aligned}$$

where $\delta u_L = \delta \mathbf{u} \cdot \mathbf{e}_L$, $\delta u_T = \delta \mathbf{u} \cdot \mathbf{e}_T$, and \mathbf{e}_L and \mathbf{e}_T are unit vectors parallel and orthogonal to the separation vector \mathbf{r} . The probability distribution function (PDF) of velocity increments is denoted by $P(\delta \mathbf{u})$ and structure functions are the statistical moments of $P(\delta \mathbf{u})$.

4.1.2 Second-order structure functions

The second-order velocity longitudinal structure functions are defined as

$$D_{LL}(r) = \langle \delta u_L \delta u_L \rangle, \quad D_{TT}(r) = \langle \delta u_T \delta u_T \rangle, \quad D_{LT}(r) = \langle \delta u_L \delta u_T \rangle \quad (1)$$

where local isotropy has been assumed, $r = |\mathbf{r}|$, and $\langle \cdot \rangle$ denotes an average over all position vectors \mathbf{x} in the domain. Local isotropy means that $D_{LT}(r) = 0$.

In isotropic turbulence, the incompressibility condition links D_{TT} and D_{LL} by

$$D_{TT}(r) = D_{LL}(r) + \frac{r}{d-1} \frac{d}{dr} D_{LL}(r) \quad (2)$$

where $d = 2$ for 2D turbulence and $d = 3$ for 3D turbulence.

3D turbulence relations

In the inertial range of isotropic 3D turbulence

$$\begin{aligned}D_{LL}(r) &= C_K \epsilon^{2/3} r^{2/3} \\ D_{TT}(r) &= \frac{4}{3} D_{LL}(r)\end{aligned} \quad (3)$$

where $C_K \approx 2$ is the Kolmogorov constant and ϵ is the eddy dissipation rate.

2D turbulence relations

For fully developed 2D isotropic turbulence analogous relations can be written ([Lindborg, 1999](#))

$$\begin{aligned} D_{LL}(r) &= C_K |\epsilon_{2D}|^{2/3} r^{2/3} \\ D_{TT}(r) &= \frac{5}{3} D_{LL}(r) \end{aligned} \quad (4)$$

where ϵ_{2D} is analogous to ϵ , but because in 2D turbulence ϵ_{2D} is negative, the absolute value is used.

Complete second-order structure function

The complete second-order structure function for d -dimensional turbulence is defined by

$$D_2(r) \equiv D_{LL}(r) + (d-1) D_{TT}(r) \quad (5)$$

4.1.3 Third-order structure functions

The third-order structure function is decomposed into diagonal

$$D_{LLL}(r) = \langle \delta u_L \delta u_L \delta u_L \rangle \quad (6)$$

$$D_{LTT}(r) = \langle \delta u_L \delta u_T \delta u_T \rangle \quad (7)$$

and off-diagonal components

$$D_{LLT}(r) = \langle \delta u_L \delta u_L \delta u_T \rangle \quad (8)$$

$$D_{TTT}(r) = \langle \delta u_T \delta u_T \delta u_T \rangle \quad (9)$$

[Mahrt and Gamage \(1987\)](#) and [Lindborg and Cho \(2001\)](#) report studies of the off-diagonal components. In this paper only the diagonal components are considered.

The total third-order structure function for d -dimensional isotropic turbulence is defined by

$$D_3(r) \equiv D_{LLL}(r) + (d-1) D_{LTT}(r) \quad (10)$$

Kolmogorov expressed the Kármán-Howarth equation ([Kármán and Howarth, 1938](#)) in terms of structure functions, and obtained an equation linking D_{LLL} with D_{LL} ([Kolmogorov, 1941](#)). In the inertial range, this equation reduces to the Kolmogorov *four-fifths law*: $D_{LLL}(r) = -\frac{4}{5}\epsilon r$, which requires fewer assumptions than relation (3) and hence is

more fundamental (*Frisch, 1995; Lindborg, 1996*). The four-fifths law is a special case of a more general energy flux equation, given by

$$D_3(r) = -\frac{4}{3}\epsilon r \quad (11)$$

for 3D turbulence (*Lindborg, 1996; Antonia et al., 1997*), and by

$$D_3(r) = -2\epsilon_2 D r \quad (12)$$

for 2D turbulence *Lindborg (1999)*.

The *skewness* or asymmetry of $P(\delta\mathbf{u})$ is given by

$$S = \frac{D_3}{D_2^{3/2}} \quad (13)$$

It is easy to show that for isotropic 3D (2D) turbulence, S is negative (positive) and constant.

4.2 Application to scatterometer winds

Scatterometer wind vectors are organized in a swath grid whose axes are aligned parallel (along-swath) and perpendicular (cross-swath) to the satellite ground track. Each grid point is at the center of a square called a wind vector cell (WVC), and each row of WVCs corresponds to a single cross-track cut of the measurement swath. The swath is inclined at an angle α relative to the North-South axis given by $\alpha = \pm |\arctan(1/\cos\phi \tan\Theta)|$, where ϕ is the latitude and $\Theta = 98.6^\circ$ is the satellite inclination angle; α is positive for the ascending pass (South-to-North), and negative for the descending pass (North-to-South).

Wind vectors are given in terms of horizontal wind speed U and wind direction ϕ_0 measured clockwise from North (oceanographic convention). They are presented in a cross-swath – along-swath coordinate system (x_c, x_a) . In an along-swath analysis, samples from each orbit are selected consisting of wind vectors with the same cross-swath coordinate (i.e., same x_c) and whose latitude and longitude are within the region of interest. Wind vectors that failed quality control were treated as missing data. After expressing wind direction counter-clockwise from East: $\phi_u = \pi/2 - \phi_o$, longitudinal and transverse wind components are calculated as

$$u_{La} = U \sin(\phi_u - \alpha) \quad (14)$$

$$u_{Ta} = -U \cos(\phi_u - \alpha) \quad (15)$$

where the subscript a is used to indicate that the separation vector is parallel to the x_a -axis (i.e., an along-swath analysis).

In this paper we carry out an along-swath analysis. Velocity differences are taken along-track

$$\begin{aligned} \delta u_{La} &= u_{La}(x_a + r) - u_{La}(x_a) \\ \delta u_{Ta} &= u_{Ta}(x_a + r) - u_{Ta}(x_a) \end{aligned}$$

The along-swath one-dimensional component structure functions are defined by

$$D_{LLa}(r) = \langle \delta u_{La} \delta u_{La} \rangle, \quad D_{TTa}(r) = \langle \delta u_{Ta} \delta u_{Ta} \rangle, \quad D_{LTa}(r) = \langle \delta u_{La} \delta u_{Ta} \rangle \quad (16)$$

and

$$D_{LLLa}(r) = \langle \delta u_{La} \delta u_{La} \delta u_{La} \rangle, \quad D_{LTTa}(r) = \langle \delta u_{La} \delta u_{Ta} \delta u_{Ta} \rangle \quad (17)$$

where $\langle \cdot \rangle = (1/N) \sum_{i=1}^N (\cdot)$ denotes a regional average over a one-month period, and N is the number of velocity differences at scale r .

5 Results

Our objective is to characterize the structure and variability of turbulence in terms of the observed skewness

$$S_a = \frac{D_{3a}}{D_{2a}^{3/2}} \quad (18)$$

where in the framework of 2D turbulence theory

$$D_{2a}(r) = D_{LLa}(r) + D_{TTa}(r) \quad (19)$$

$$D_{3a}(r) = D_{LLLa}(r) + D_{LTTa}(r) \quad (20)$$

Results for D_{LLa} and D_{TTa} have been presented in *King et al. (2013)*. Therefore here we only show the slope of D_{2a} , denoted by β , estimated from fits in log-log space over the range 50 to 250 km. Figure 6 shows curves of β , one for each wind product. The curves of β are parallel but with a systematic difference in magnitude due to differences in noise level, spatial filtering, and ambiguity removal. ASCAT-12.5 has the smallest slopes and SeaWinds-KNMI the steepest. Overall, β varies between $2/3$ and $3/2$, corresponding to spectra with power laws varying between $k^{-5/3}$ and $k^{-2.5}$, consistent with earlier spectral analyses. Furthermore, β exhibits a regional and seasonal dependence that reflects the regional and seasonal characteristics of the tropical Pacific (see section 2).

The dependence of D_{3a} on r is shown in Figures 7 (January) and 8 (August). These figures show that D_{3a} varies in magnitude and in sign across the tropical Pacific. There is also some dependence on wind product. There is little difference between ASCAT-25 and ASCAT-12.5 in either rainy or dry regions. On the other hand, there are significant differences between the three SeaWinds products in rainy regions but not in the dry regions. This is not surprising since SeaWinds is sensitive to rain, but the differences are also the result of differences in the algorithms used to produce the three SeaWinds products. SeaWinds and ASCAT products hardly differ in the dry regions, but show significant differences in rainy regions. The differences are partly due to processing differences, but also sampling differences: the QuikSCAT and MetOp-A satellites do not pass over the same region at the same time of day. Finally we note that there are large differences between scatterometer and NWP winds in both rainy and dry regions (except in CPS and EPS).

Comparison of D_{3a} (Figs. 7 and 8) with rain-rate (Figs. 4 and 5) shows an interesting correlation. Broadly speaking, D_{3a} is negative in rainy regions and positive in dry regions. However, note the intriguing exception of positive D_{3a} in WPE-January. Some other regions also lack a clear correlation: $D_{3a} \approx 0$ in WPN-August, EPE-January, and CPS- and EPS-August. The latter two cases are probably due to the light and steady winds that occur in these regions, while EPE-January is a transition month between the cold/dry and warm/wet seasons in the east Pacific.

We now consider S_a . According to theory, $S_a = \text{constant}$ in the inertial range of isotropic turbulence. However, Figures 9 and 10 show that S_a is approximately independent of r in the rainy regions. In the dry regions, S_a increases with r up to about 200-300 km

and then flattens. Similar results were obtained for different months of the year. As a compromise, it was decided to represent the temporal variation of S_a by its value at 300 km: $S_a^* \equiv S_a(300 \text{ km})$.

Figure 11 shows the monthly time series of S_a^* . Interestingly, the curves for different wind products do not differ by much. In order to better examine the correlation with rain, monthly-averaged SRAD rain rates are also shown. There is an excellent S_a^* -rain correlation in the dry regions, with EPE the best example. Here $S_a^* > 0$ during the cold/dry season, and $S_a^* < 0$ during the warm/wet season. There is also a S_a^* -rain correlation in the rainy regions, but it is more complex: S_a^* is nearly constant (≈ -0.1) in CPN and EPN, but varies between -0.1 and 0.02 in the WP regions. Why the correlation exists in some regions better than in others is discussed below.

Figure 12 compares S_a^* for the NWP winds and 12.5 km scatterometer winds. In general, NWP and scatterometer results are in fairly close agreement in both magnitude and sign, except in EPS from May to October. Since the NWP forecast models miss the small scale structures resolved by scatterometers, this is an intriguing result.

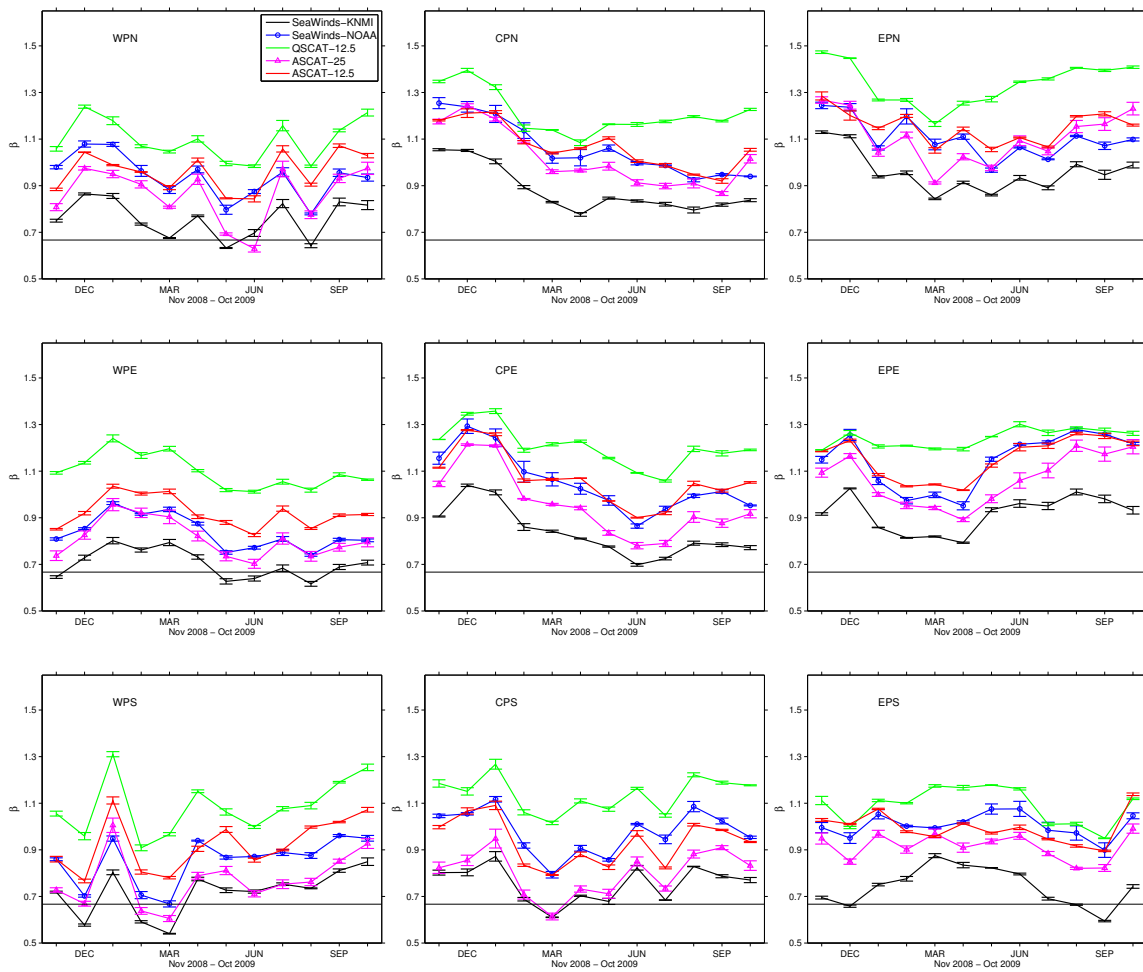


Fig. 6: Structure function slope β estimated from fits to $\log D_{2a}$ vs. $\log r$ over the range 50-250 km. Error bars show the root-mean square deviation.

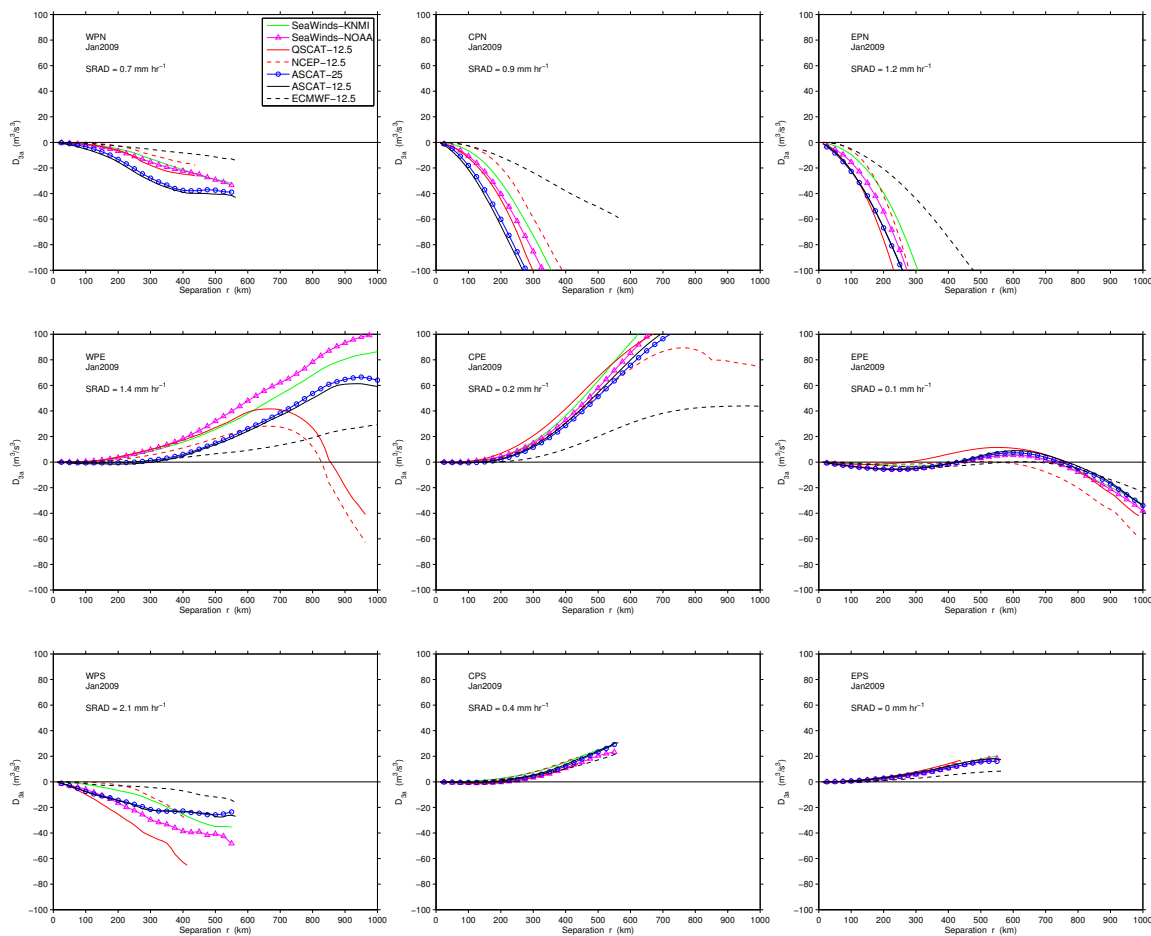


Fig. 7: D_{3a} vs r (January 2009).

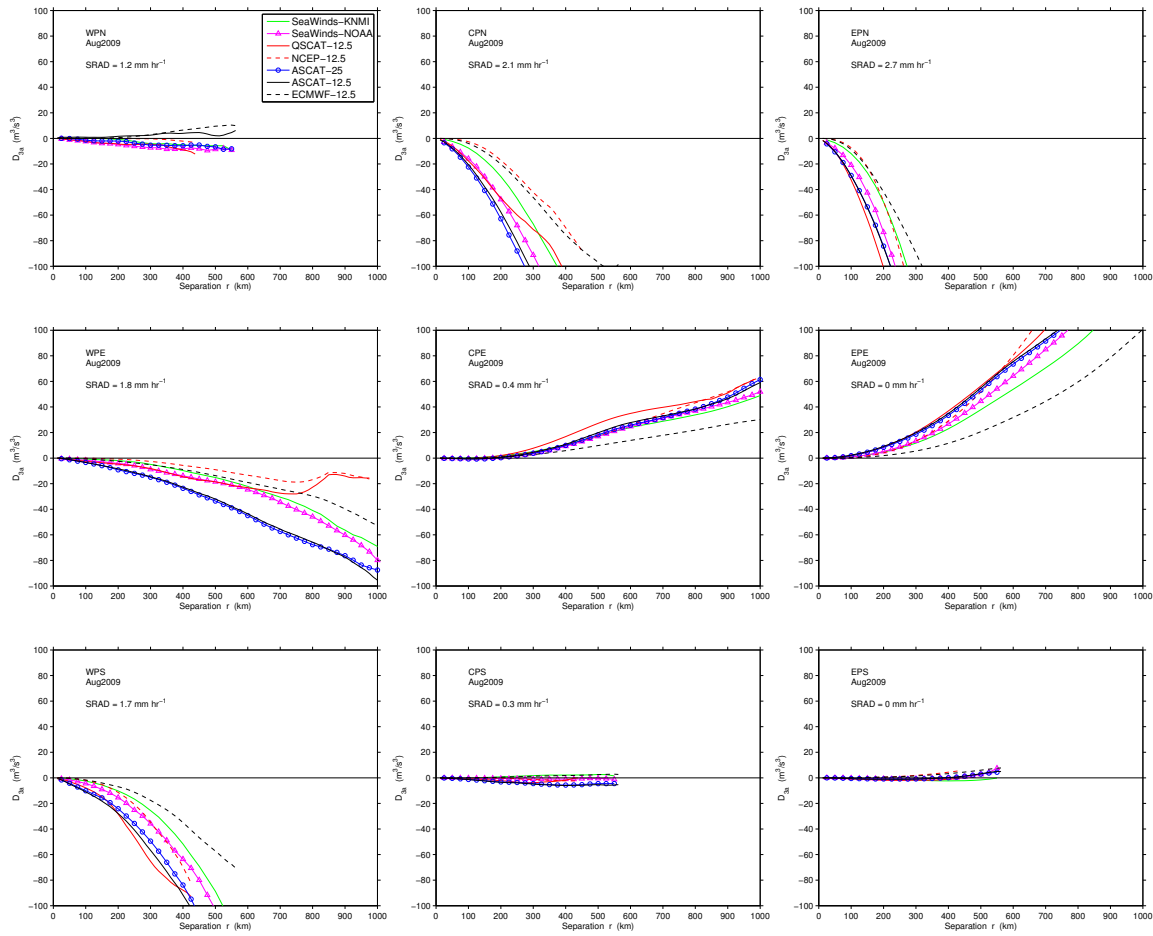


Fig. 8: D_{3a} vs separation r . August 2009 — all regions. The line types and colors are the same as in Fig. 7.

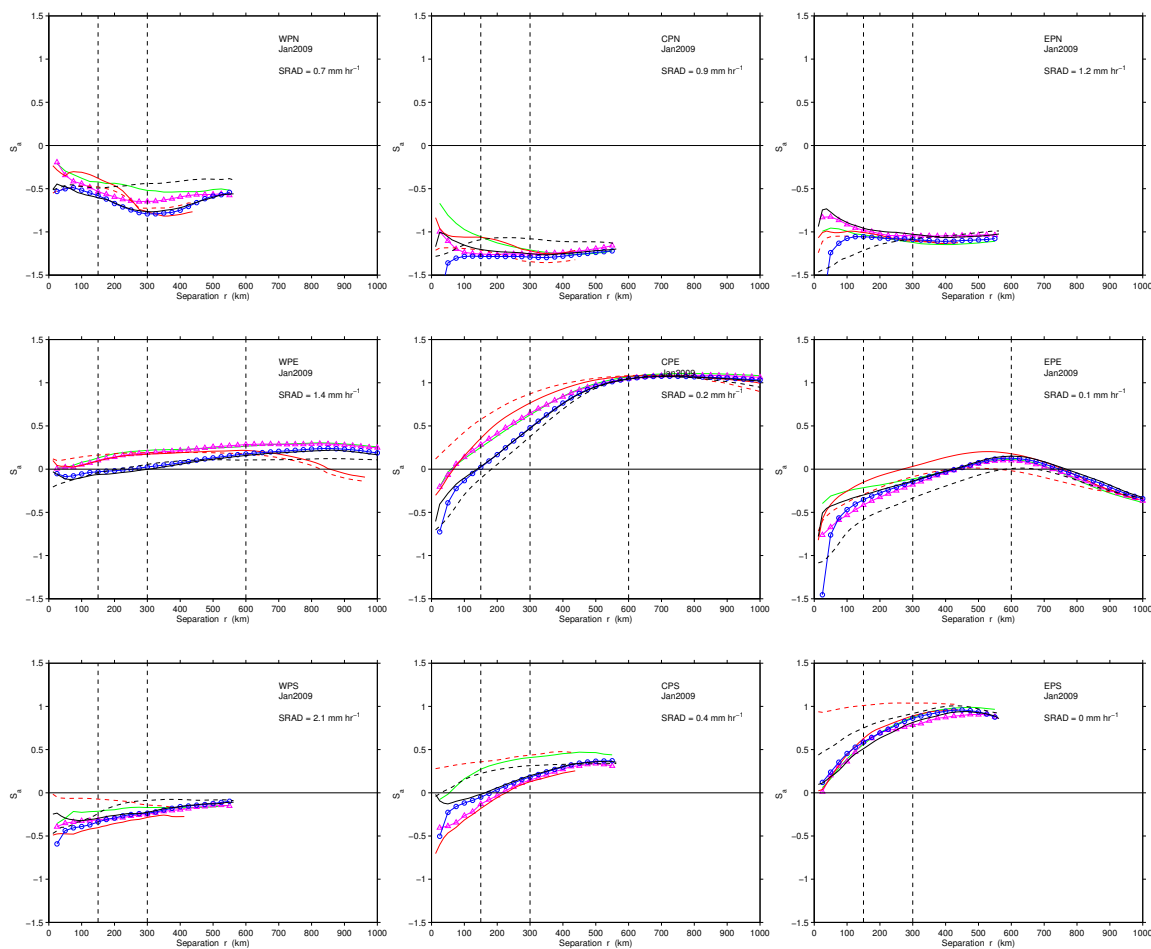


Fig. 9: Skewness vs separation r . January 2009 — all regions. The line types and colors are the same as in Fig. 7.

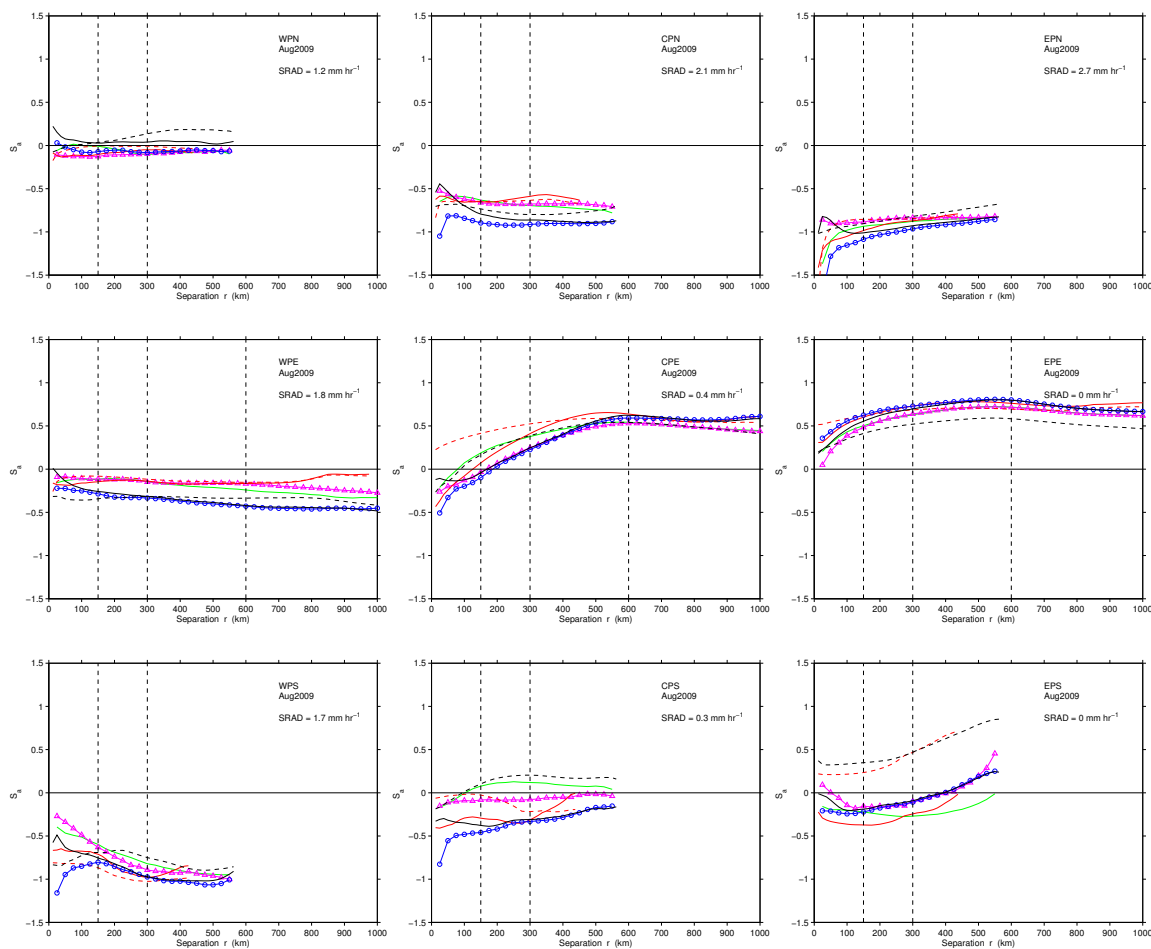


Fig. 10: Skewness vs separation r . August 2009 — all regions. The line types and colors are the same as in Fig. 7.

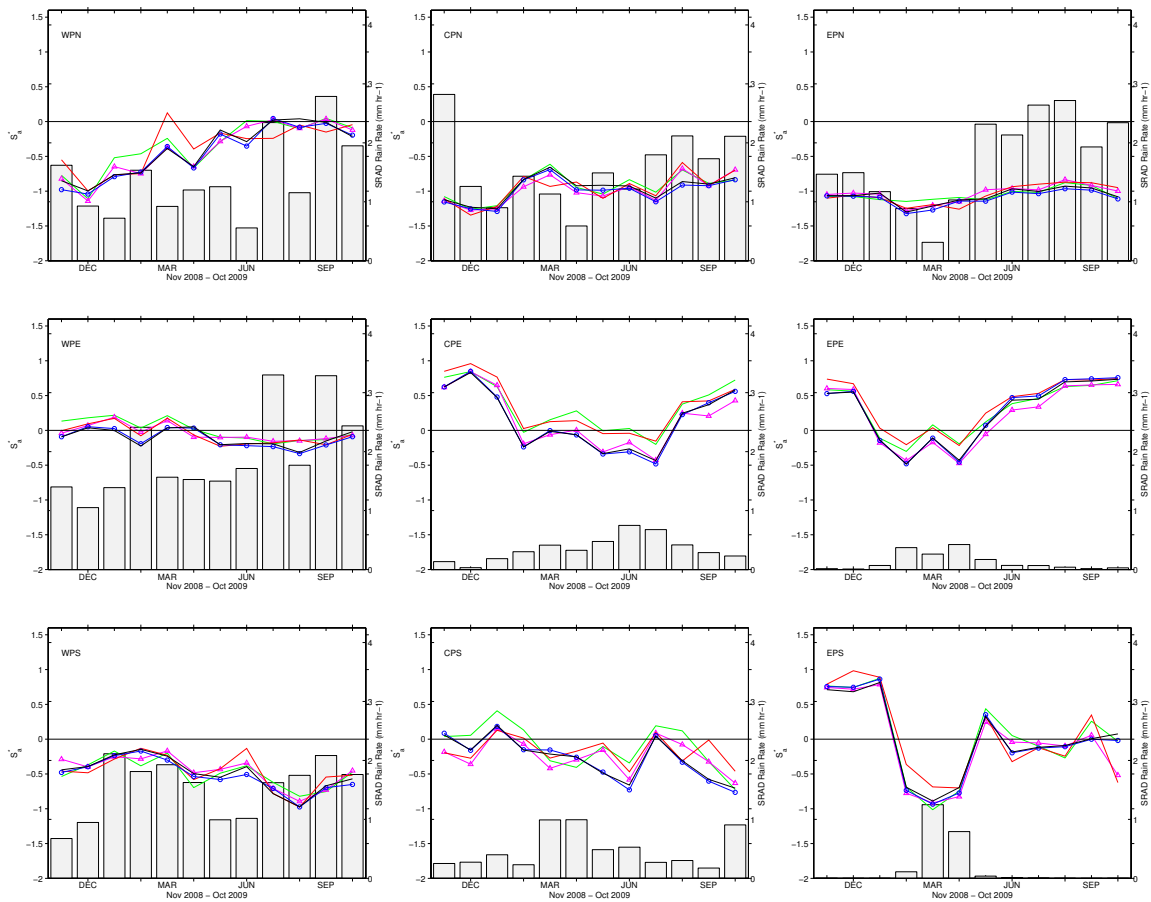


Fig. 11: Time series of S_a^* (skewness at 300 km). All wind products are shown. The line types and colors are the same as in Fig. 7. The bar graph shows monthly SRAD rain-rates (see black curve in Fig. 5).

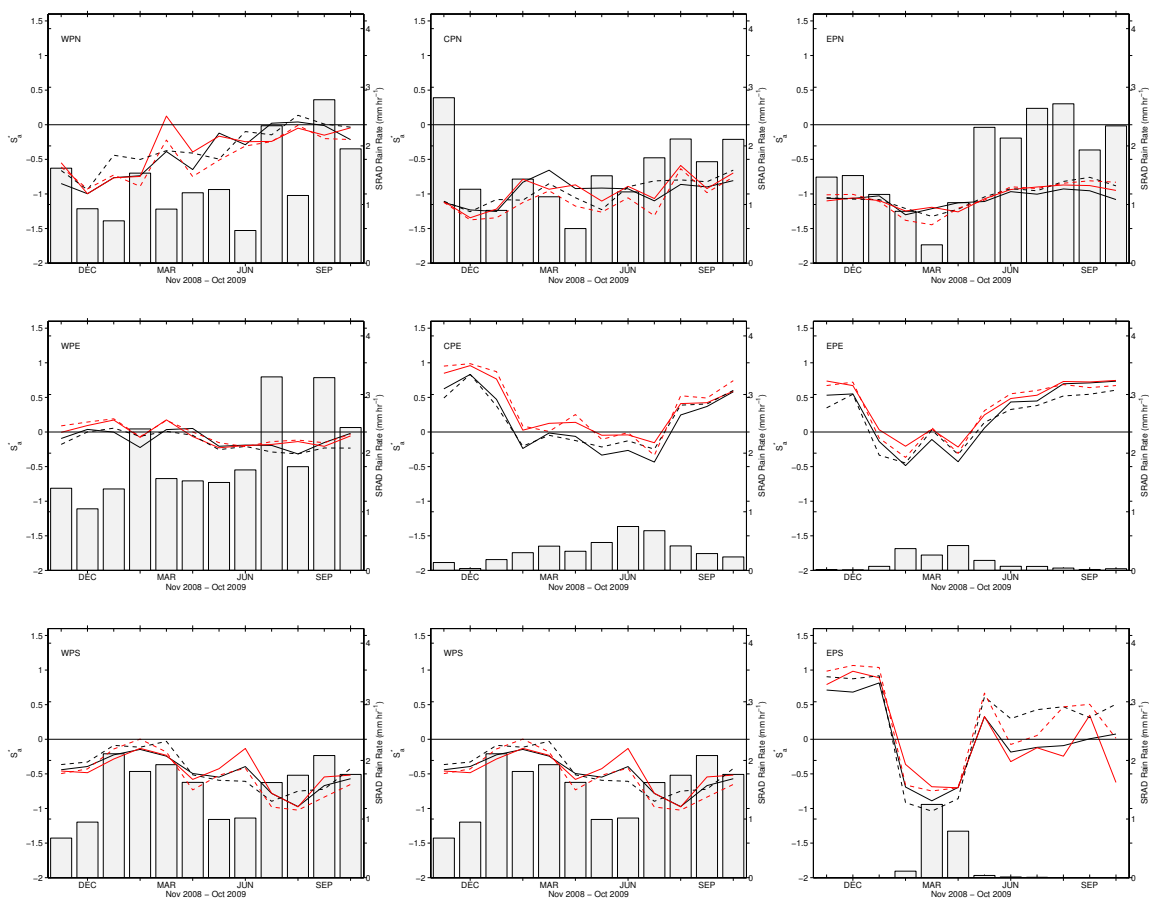


Fig. 12: As in Fig. 13, but comparison of NWP models winds with the 12.5 km products.

6 Discussion

6.1 Understanding the sign

We have found that D_{3a} and hence S_a , change sign across the tropical Pacific, implying evidence for both upscale and downscale energy transfer. We also see an intriguing correlation with rain: $S_a^* > 0$ in the dry regions when there is little or no rain, and, apart from some interesting exceptions, $S_a^* < 0$ in the rainy regions and in the wet season of the dry regions. This pattern of correlation has a straightforward explanation. Expand Eq. (20) as

$$D_{3a}(r) = \left\langle \delta u_{La} \left[(\delta u_{La})^2 + (\delta u_{Ta})^2 \right] \right\rangle \quad (21)$$

which now makes clear that the term responsible for the sign of D_{3a} is δu_{La} . A sketch of some arbitrary one-dimensional vectors $u(x)$ at discrete positions along coordinate x shows that (i) where u is converging ($\rightarrow \leftarrow$) or decelerating ($\rightarrow \rightarrow$), $\delta u = u(x+r) - u(x) < 0$, and (ii) where u is diverging ($\leftarrow \rightarrow$) or accelerating ($\rightarrow \rightarrow$), $\delta u > 0$. Therefore, where and when surface convergence/deceleration dominates, D_{3a} (and S_a^*) is almost sure to be negative. This is the case in the strongly convergent ITCZ regions CPN and EPN and in the wet seasons of the dry regions EPE and EPS. Similarly, where and when surface divergence/acceleration dominates, D_{3a} (and S_a^*) is almost sure to be positive. This happens over the cold tongue (EPE) when southerly winds blow from cool to warm ocean across the strong SST front that forms its northern boundary: a spatial acceleration ($\delta u_{La} > 0$) in the wind is created when convection over the warm water to the north of the front brings faster moving air from above closer to the surface south of the front (*Chelton et al., 2004; Small et al., 2008*, and references therein).

6.2 Decomposition of the skewness

In contrast to CPN and EPN, S_a^* varies seasonally in the WP regions and even approaches zero during the summer months. A decrease in magnitude could be due to weaker and steadier meridional winds, or equal proportions of convergence and surface divergence. To identify which plays the greater role, we decompose S_a^* into convergent and divergent fractions

$$S_a^* = S_a^{*-} + S_a^{*+} \quad (22)$$

where

$$S_a^{*-} = \frac{D_{3a}^-}{D_{2a}^{3/2}}, \quad S_a^{*+} = \frac{D_{3a}^+}{D_{2a}^{3/2}}$$

$$D_{3a}^- = \frac{1}{N} \left[\sum_{\delta u_{La} < 0} \delta u_{La} (\delta u_{La}^2 + \delta u_{Ta}^2) \right]$$

$$D_{3a}^+ = \frac{1}{N} \left[\sum_{\delta u_{La} > 0} \delta u_{La} (\delta u_{La}^2 + \delta u_{Ta}^2) \right]$$

Figure 13 shows this decomposition carried out for QSCAT-12.5 and NCEP-12.5 winds. The panels in the figure shows that S_a^{*+} is significant in the WP regions, but virtually zero in CPN and EPN. The source of the WP divergent component is probably the low-level divergence generated by mesoscale convective systems (Houze, 2004).

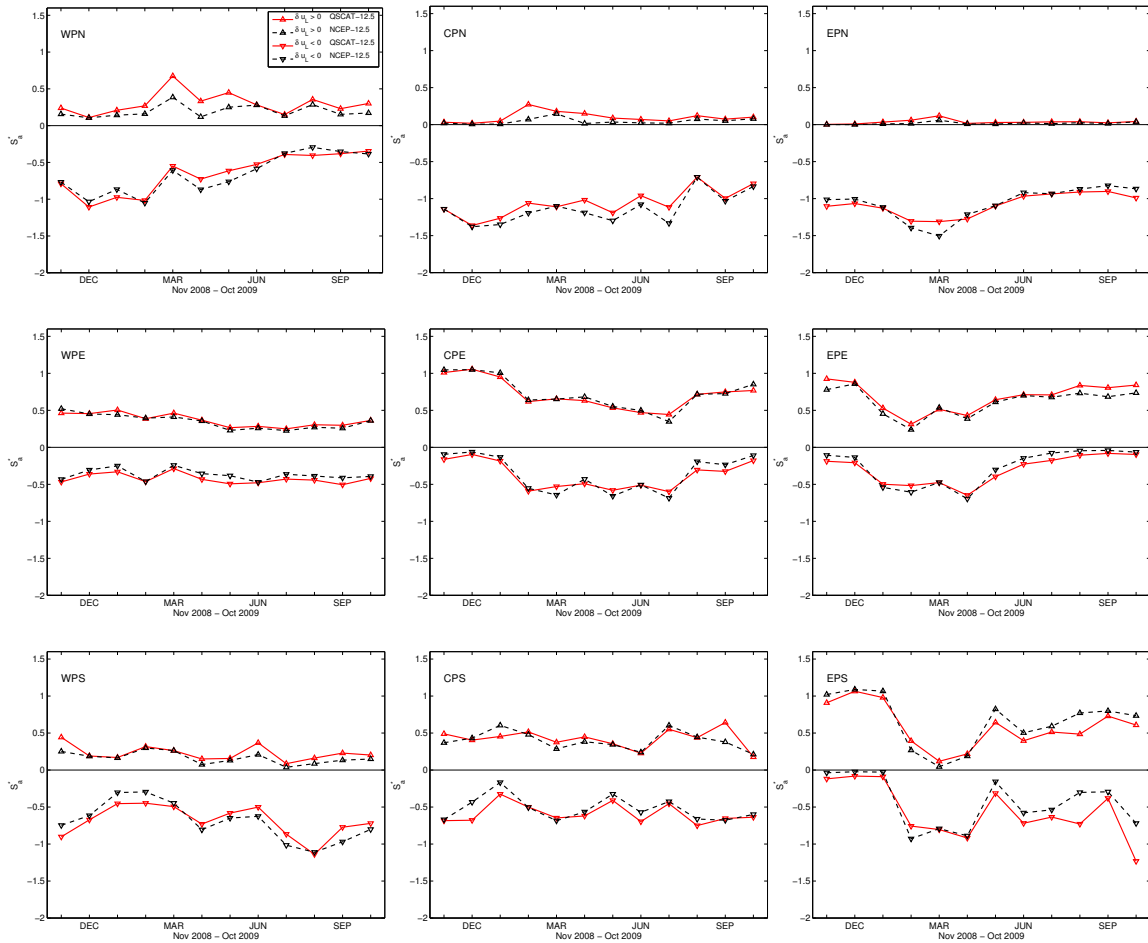


Fig. 13: Time series S_a^{*+} separated into divergent (Δ) and convergent (∇) contributions: QSCAT-12.5 (red) and NCEP-12.5 (black dashed).

6.3 Decomposition of the turbulent kinetic energy

It is also interesting to decompose the turbulent kinetic energy — not only into divergent and convergent components, but also cyclonic and anti-cyclonic components. We do this for the turbulent kinetic energy proxy $K_{ia} \equiv D_{ia}(300\text{km})$ *King et al.* (see 2013):

$$\begin{aligned} K_{La} &= K_{La}^- + K_{La}^+ \\ K_{Ta} &= K_{Ta}^- + K_{Ta}^+ \end{aligned}$$

where

$$\begin{aligned} K_{La}^- &= \frac{1}{N} \left[\sum_{\delta u_{La} < 0} \delta u_{La}^2(300\text{km}) \right] && \text{(convergent)} \\ K_{La}^+ &= \frac{1}{N} \left[\sum_{\delta u_{La} > 0} \delta u_{La}^2(300\text{km}) \right] && \text{(divergent)} \end{aligned}$$

and

$$\begin{aligned} K_{Ta}^- &= \frac{1}{N} \left[\sum_{\delta u_{Ta} < 0} \delta u_{Ta}^2(300\text{km}) \right] && \text{(anti-cyclonic)} \\ K_{Ta}^+ &= \frac{1}{N} \left[\sum_{\delta u_{Ta} > 0} \delta u_{Ta}^2(300\text{km}) \right] && \text{(cyclonic)} \end{aligned}$$

Figures 14 and 15 show the decomposition for ASCAT-12.5 (black) and QSCAT-12.5 (red) winds. Fig. 14 illustrates the level and variability of surface divergence and convergence, while Fig. 15 illustrates interesting variability in the rotation of the wind field. These figures were checked for consistency with the QuikSCAT wind divergence and wind curl climatology published by *Risien and Chelton* (2008) using subsets extracted from the maps published on the SCOW web site (<http://cioss.coas.oregonstate.edu/scow/index.html>). The results were also found to be consistent with work by Jerome Patoux, Angel F. Adames-Corraliza and Ralph C. Foster, who decomposed scatterometer winds into irrotational and nondivergent components using a wind partitioning method (*Patoux et al.*, 2010; *Patoux and Foster*, 2012, and references therein). Their work was presented at the International Ocean Vector Wind Science Team meeting in 2012 (IOVWST 2012). The IOVWST presentation is available at coaps.fsu.edu/scatterometry/meeting/docs/2012.../patoux_mjo.pdf (see slides 22-25).

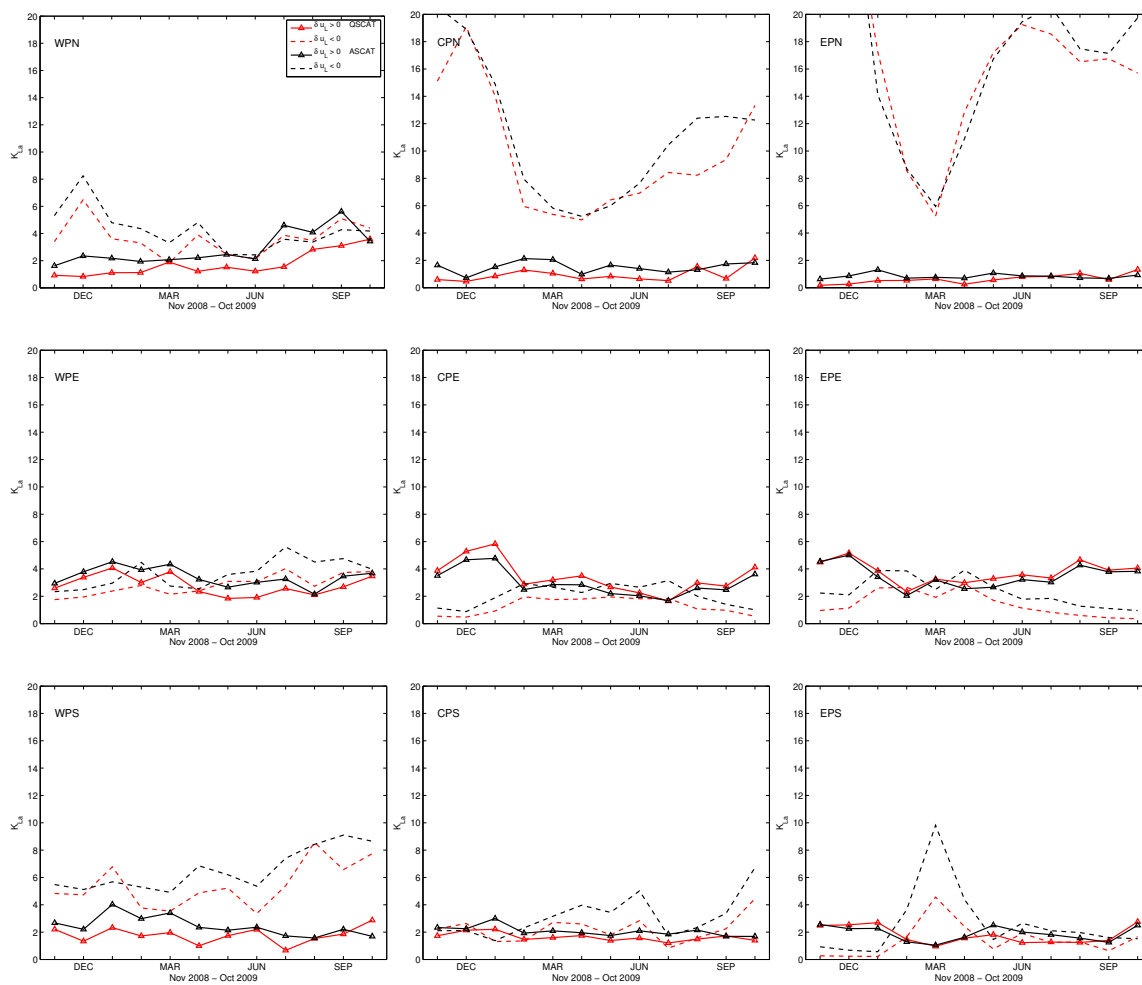


Fig. 14: Decomposition of K_{La} into divergent (Δ) and convergent (dashed line) contributions for ASCAT-12.5 (black) and QSCAT-12.5 (red).

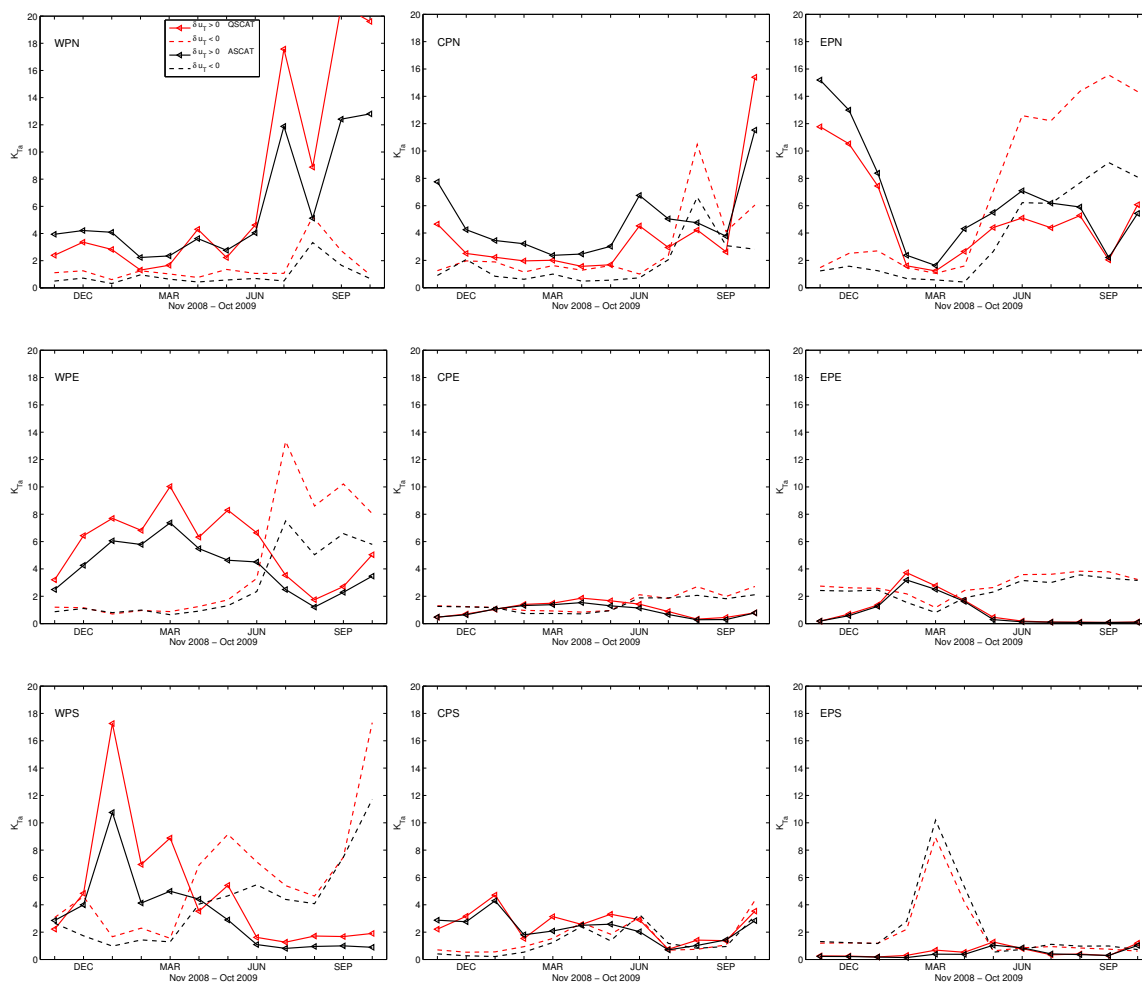


Fig. 15: Decomposition of K_{Ta} into cyclonic (\triangleleft) and anti-cyclonic (dashed) contributions for ASCAT-12.5 (black) and QSCAT-12.5 (red).

6.4 Diurnal effects

In Fig. 7 the QSCAT-12.5 structure function in WPE reaches a maximum near 600 km and goes negative at about 850 km. This is quite different from the behavior shown by all other scatterometer products. After some checking we found that the differences were mainly due to the evening pass, as can be seen by comparing the panels in Figure 16. It is also interesting to note that the results for the ASCAT morning pass is similar to the QuikSCAT evening pass, and the ASCAT evening pass more similar to the QuikSCAT morning pass. Thus these results illustrate important diurnal effects.

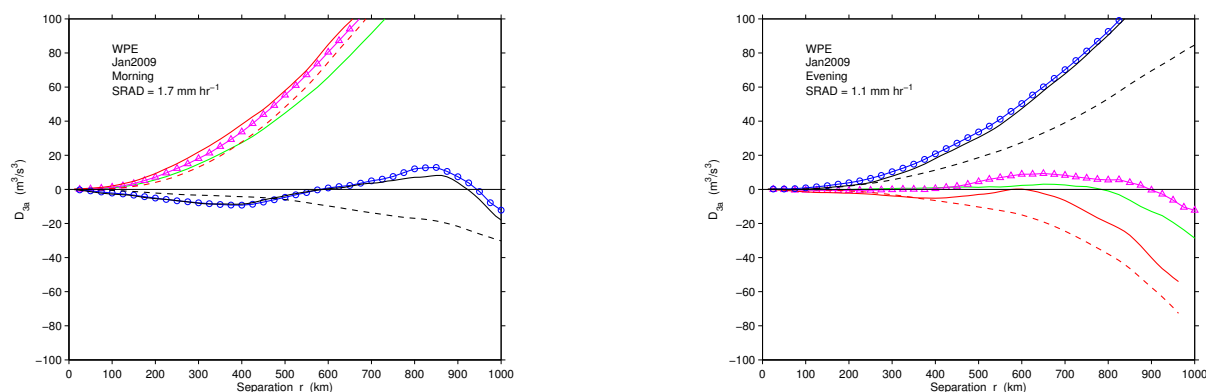


Fig. 16: Comparison of D_{3a} for the morning and evening passes in WPE January. Note that the QuikSCAT satellite crosses the equator at 06:30 and 18:30, while MetOp-A crosses three hours later at 09:30 and 21:30. The line types and colors are the same as in Fig. 7.

6.5 PDFs of velocity increments

Structure functions are the statistical moments of the probability distribution function of velocity increments, denoted by $P(\delta\mathbf{u})$. The second-order structure function is a measure of its width and the skewness its asymmetry. Thus an alternative to investigating specific statistical moments is to directly investigate $P(\delta\mathbf{u})$. The purpose here is two-fold: (i) to show how $P(\delta\mathbf{u})$ varies regionally and seasonally in the tropical Pacific, and (ii) to compare NWP and scatterometer $P(\delta\mathbf{u})$. For convenience and clarity, we show distributions for the two velocity components at a single scale, taken to be $r = 300$ km, and only for QSCAT-12.5 and NCEP-12.5. The distributions at $r = 300$ km are denoted by $P(\delta u_{La}^*)$ and $P(\delta u_{Ta}^*)$.

The variation of $P(\delta\mathbf{u})$ by region is shown in Figures 17–22: $P(\delta u_{La}^*)$ in January (Fig. 17) and August (Fig. 18), and $P(\delta u_{Ta}^*)$ in January (Fig. 21) and August (Fig. 22). The time evolution of $P(\delta u_{La}^*)$ and $P(\delta u_{Ta}^*)$ is shown for the regions WPS and EPE in Figures 19–24. These figures give a different and more detailed view of the characteristics of the motion (convergent/divergent, cyclonic/anticyclonic) and what is present in scatterometer by not NWP winds. Similar plots comparing $P(\delta\mathbf{u})$ for QuikSCAT and ASCAT could be made. However, one must take into consideration that the two satellites do not observe the same winds.

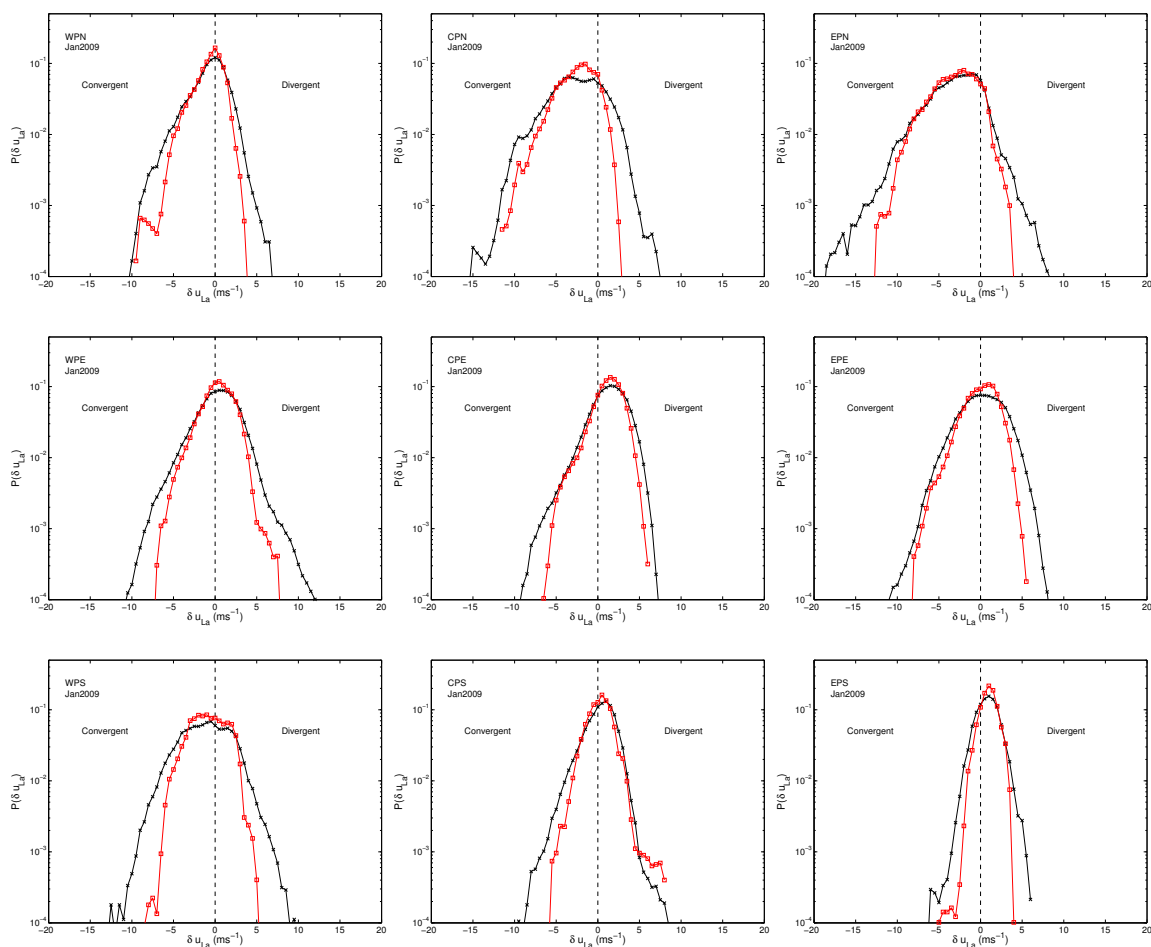


Fig. 17: Regional variation of $P(\delta u_{La}^*)$, the longitudinal velocity increment PDF at $r = 300$ km, for January 2009: QSCAT-12.5 (—×—) ; NCEP-12.5 (—□—).

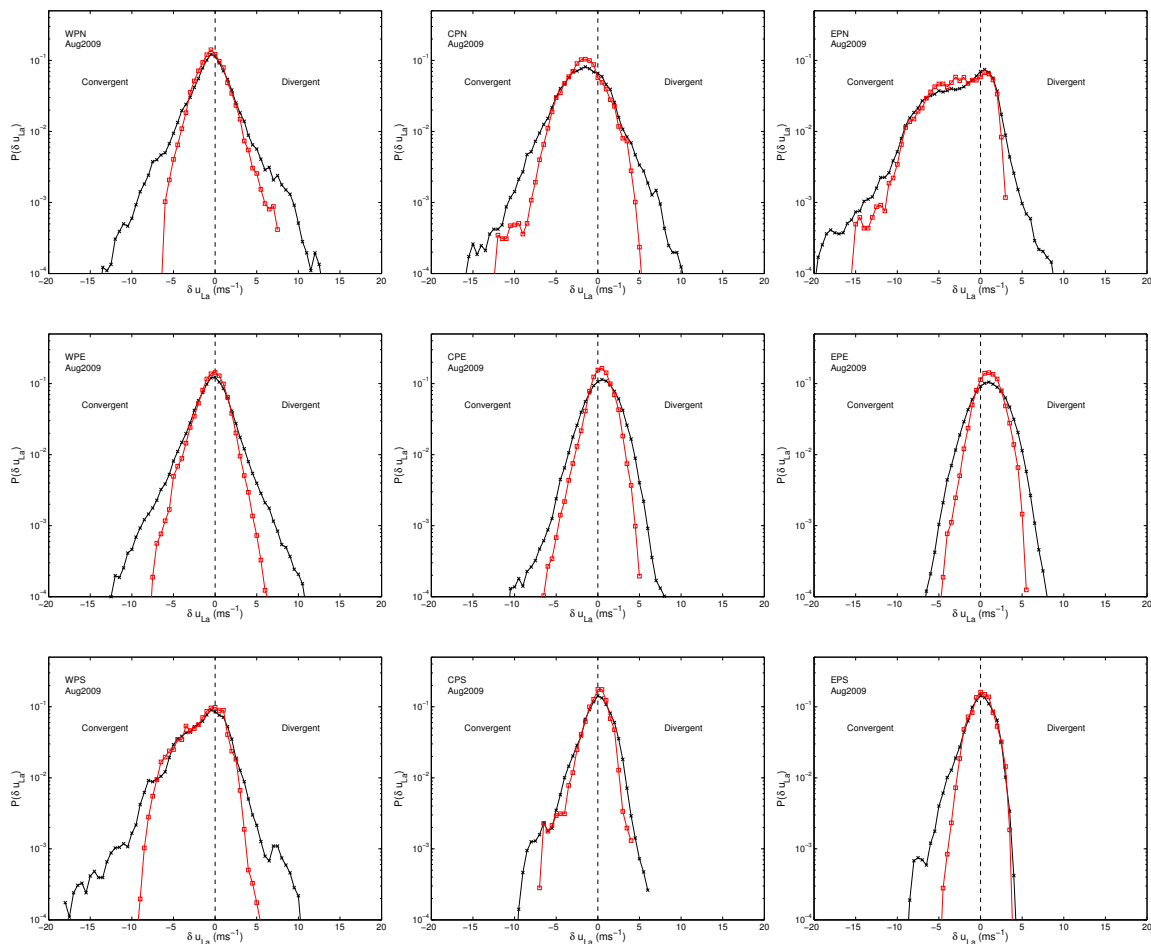


Fig. 18: Regional variation of $P(\delta u_{La}^*)$, the longitudinal velocity increment PDF at $r = 300$ km, for August 2009: QSCAT-12.5 (—×—) ; NCEP-12.5 (—□—).

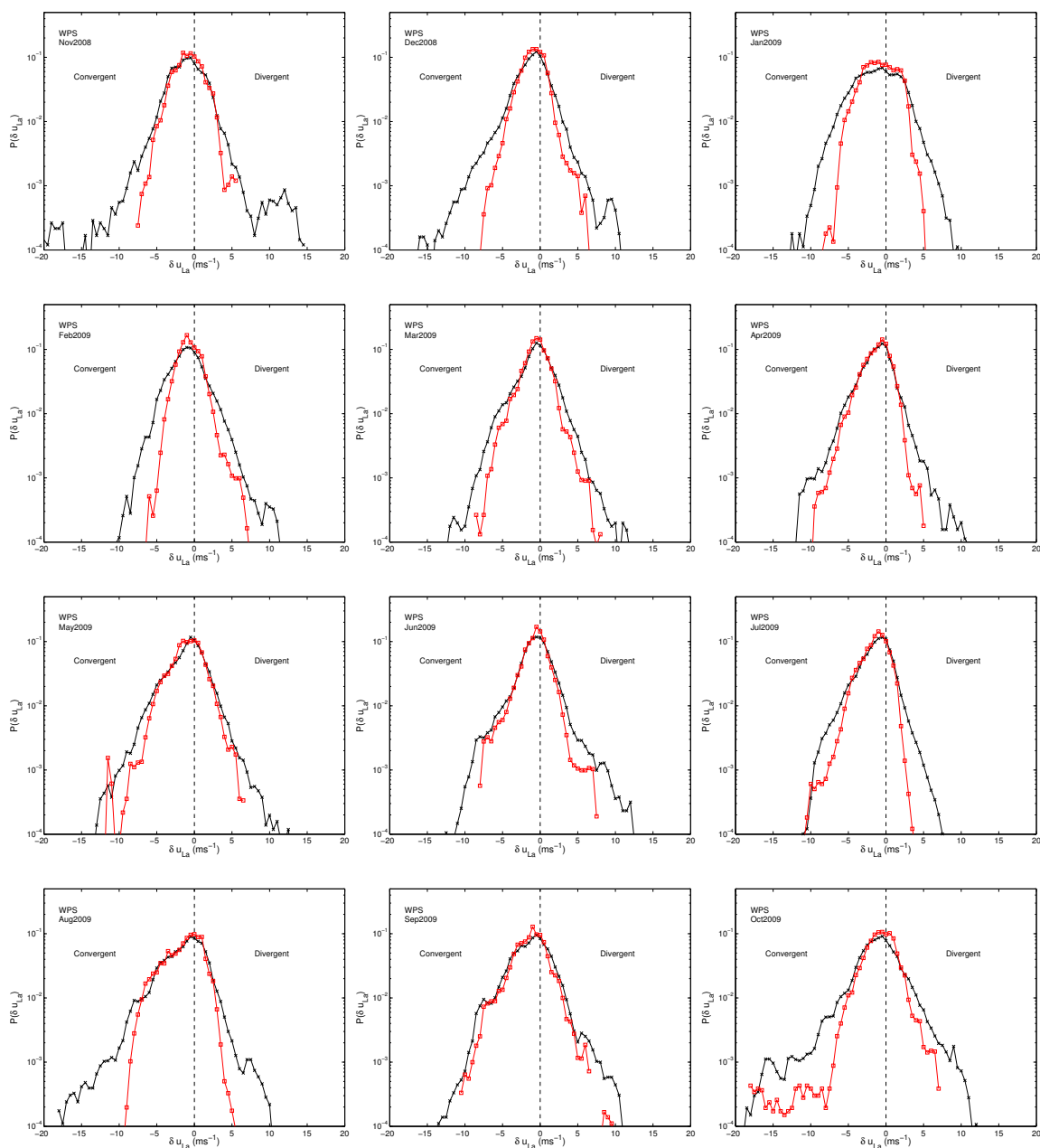


Fig. 19: Time evolution of $P(\delta u_{La}^*)$ for the WPS: QSCAT-12.5 (—×—) ; NCEP-12.5 (—□—).

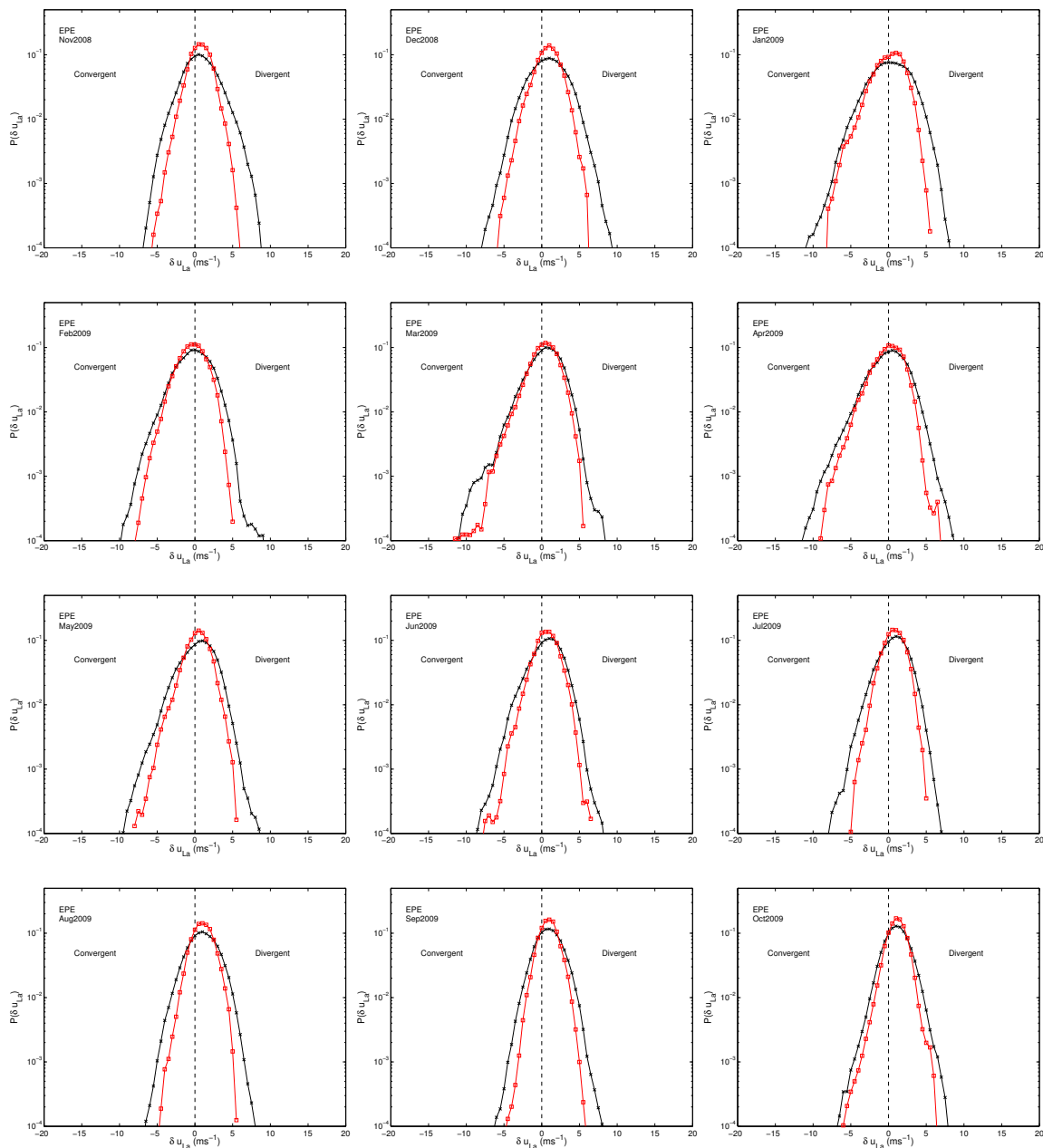


Fig. 20: Time evolution of $P(\delta u_{La}^*)$ for the EPE: QSCAT-12.5 ($-\times-$) ; NCEP-12.5 ($-\square-$).

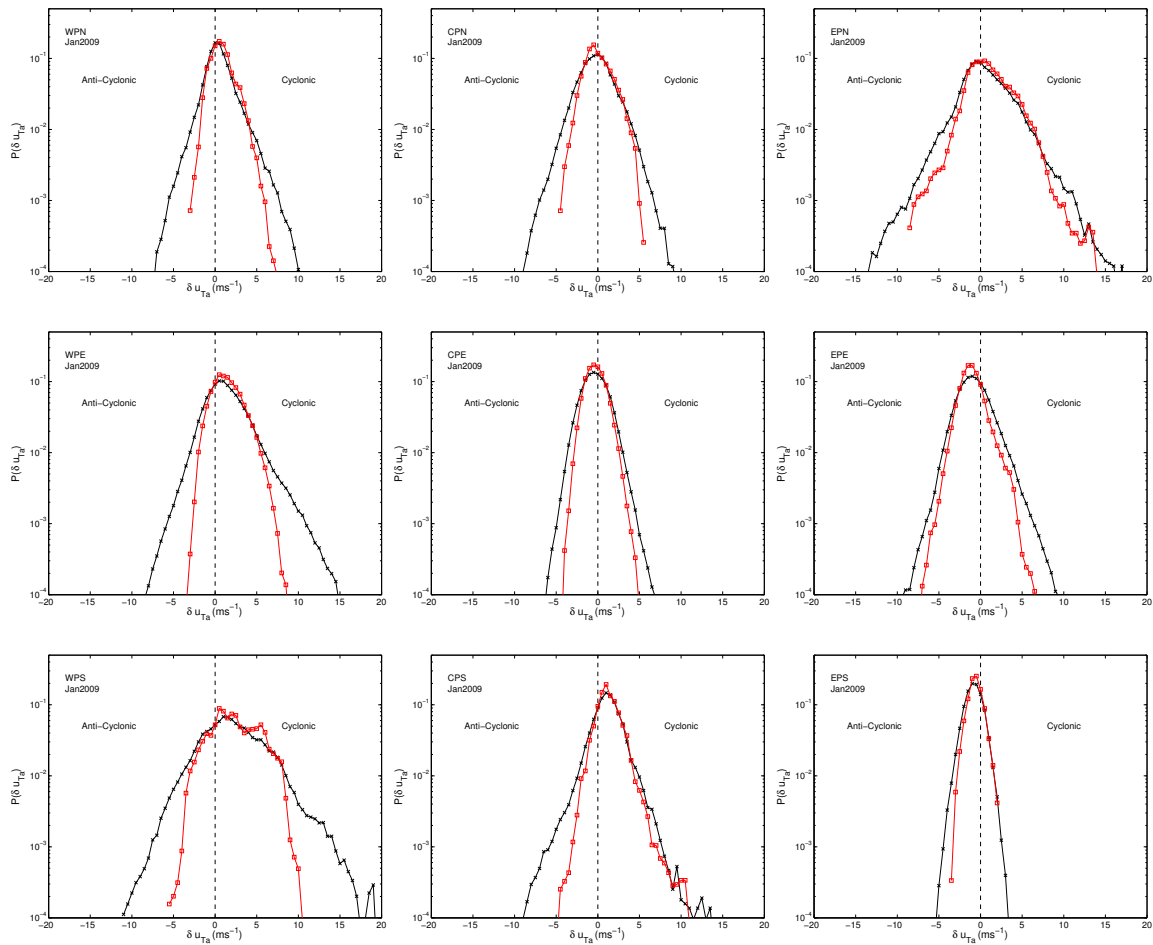


Fig. 21: Regional variation of $P(\delta u_{Ta}^*)$, the transverse velocity increment PDF at $r = 300$ km, for January 2009: QSCAT-12.5 ($-\times-$) ; NCEP-12.5 ($-\square-$).

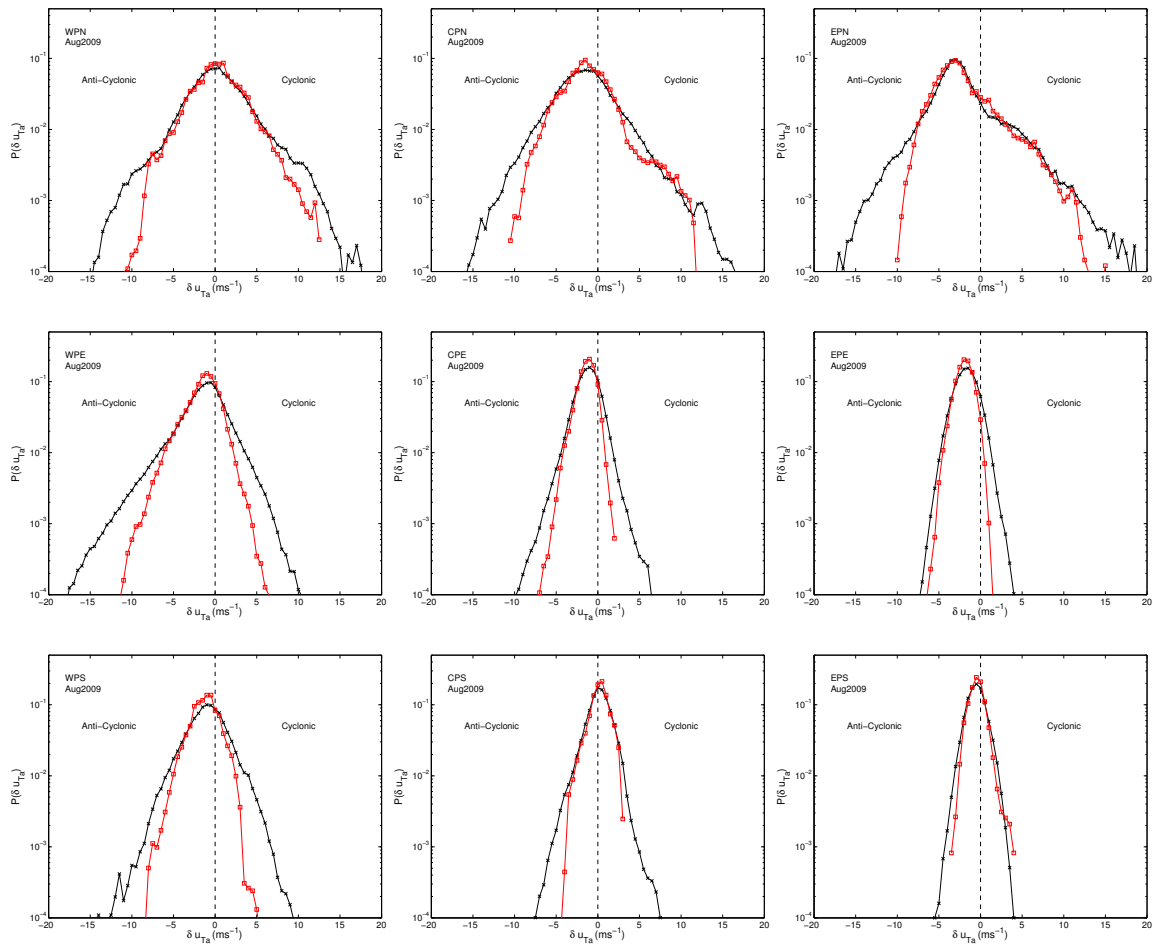


Fig. 22: Regional variation of $P(\delta u_{Ta}^*)$, the transverse velocity increment PDF at $r = 300$ km, for August 2009: QSCAT-12.5 ($-\times-$) ; NCEP-12.5 ($-\square-$).

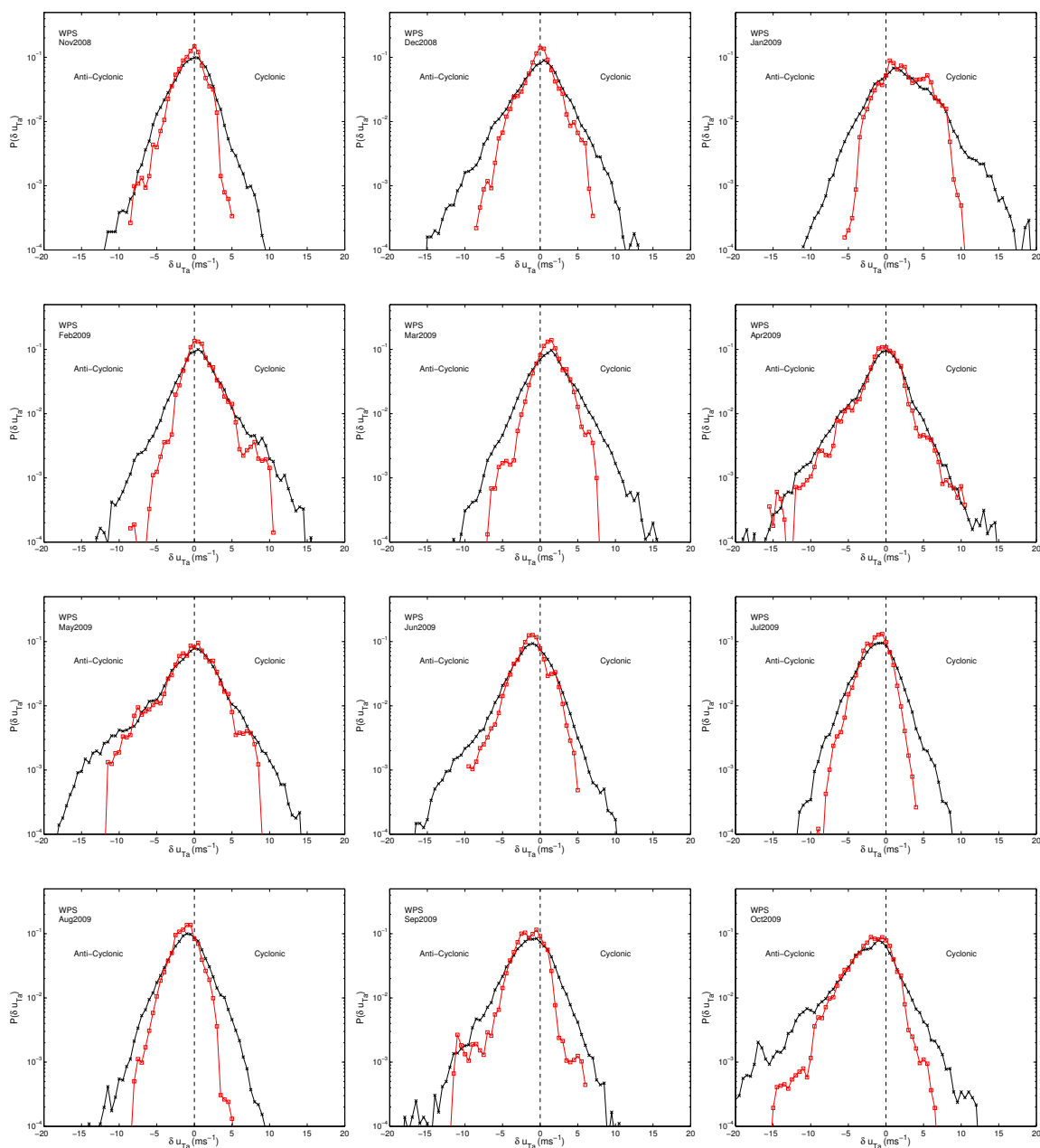


Fig. 23: Time evolution of $P(\delta u_{Ta}^*)$ for the WPS: ($- \times -$) QSCAT-12.5; ($- \square -$) NCEP-12.5.

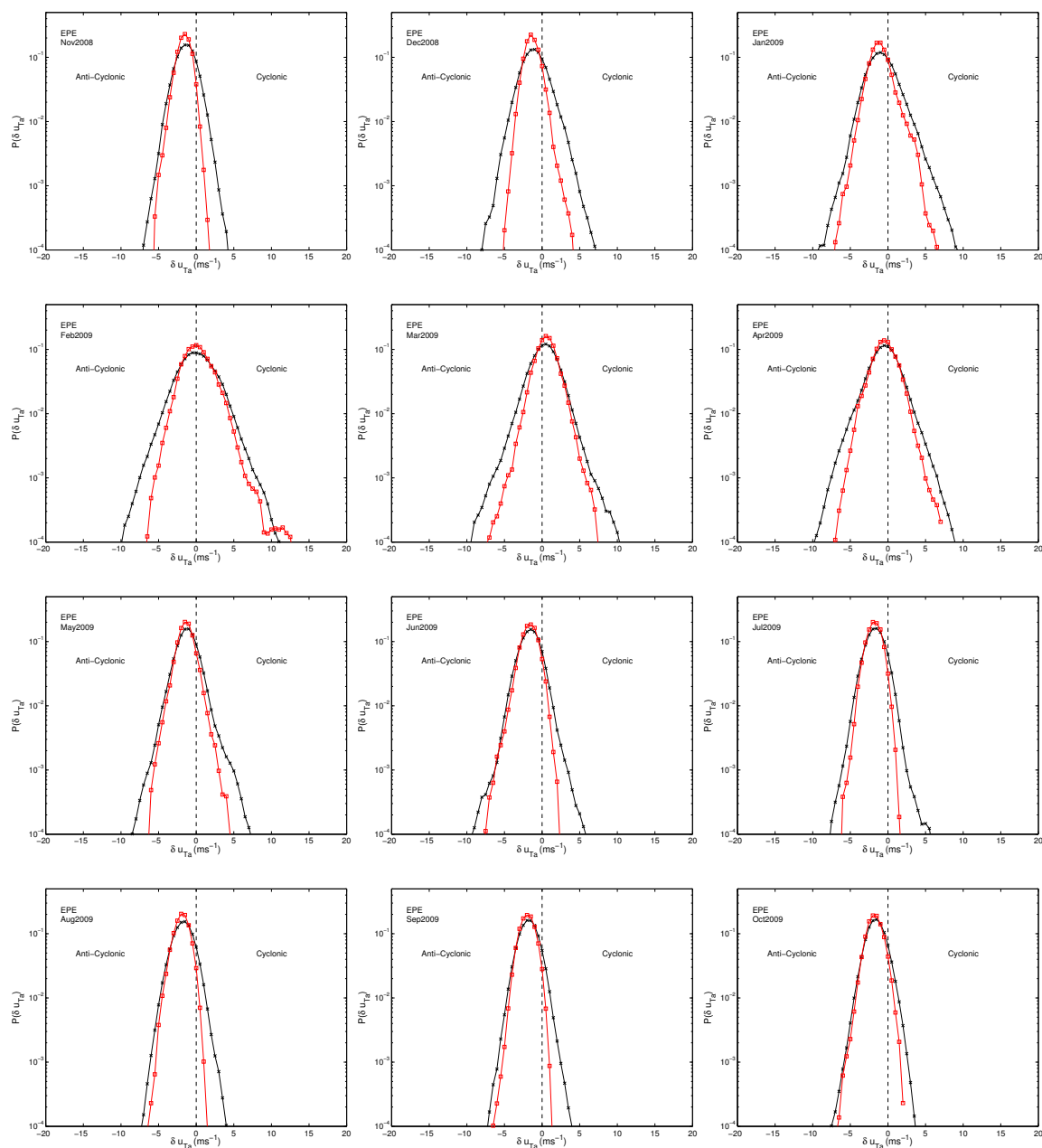


Fig. 24: Time evolution of $P(\delta u_{Ta}^*)$ for the EPE.

7 Conclusions

In this paper we have calculated third-order structure functions using winds at the bottom of the marine boundary layer measured by satellite scatterometers. According to turbulence theory, the sign of the third-order structure function, or equivalently the sign of the skewness S , identifies the direction of energy transfer, with $S < 0$ implying downscale transfer and $S > 0$ an upscale transfer. Using along-track (approximately meridional) near-surface winds inferred from scatterometer measurements by SeaWinds-on-QuikSCAT and ASCAT-on-MetOp-A, one-dimensional structure functions and skewness S_a were calculated for both rainy and dry regions in the tropical Pacific. We argued that the time evolution of S_a could be monitored using its value at 300 km, denoted by S_a^* . We found that S_a^* varied in sign and magnitude regionally and seasonally. Decomposing S_a^* into divergent (where $\delta u_{La} > 0$) and convergent (where $\delta u_{La} < 0$) components, the variability was shown to be due to the changing relative strength of convergence and divergence within a region. Thus our main result is that

- downscale signature $S_a^* < 0$ where and when surface convergence (i.e., deep convection) dominates,
- upscale signature $S_a^* > 0$ where and when surface divergence dominates
- $S_a^* \approx 0$ where and when near-equal levels of surface convergence and divergence occur during the averaging period.

The question of energy transfer in the atmospheric mesoscales is presented in the literature as if it must be “either-or”. The results presented here are inconsistent with this view. Instead we find both upscale and downscale signatures, but with relative magnitudes that vary regionally and monthly (Fig. 13). Thus the question that should be asked is: “Where, when and why is it upscale (downscale)?”.

The standard picture of energy transfer in 3D turbulence is that energy is drained from larger to smaller scales via vortex folding and stretching. In ideal 2D turbulence the actual mechanism remains controversial, but numerical studies indicate that it involves the coupling of the large-scale stress to the thinning of smaller-scale vortices ([Boffetta and Ecke, 2012](#)). The link established between S_a and surface divergence and convergence makes it difficult to interpret our results in terms of a standard 3D or 2D process. A simpler picture is one of horizontal kinetic energy being transported vertically out of the surface layer by convection ($S_a^* < 0$), or into the surface layer ($S_a^* > 0$) by low-level divergence. In the west Pacific, low-level divergence is generated by mesoscale convective systems, while in the east Pacific it is generated by spatial acceleration of winds across a strong SST gradient. An additional contribution to horizontal energy transfer may come from wind-waves (energy loss) and wave-driven-winds (energy gain) ([Hanley et al., 2010](#)). Perhaps the energy transfer by these air/sea interactions could be quantified in terms of the third-order structure function?

A more general way to study mesoscale turbulence is through velocity increment PDFs, $P(\delta \mathbf{u})$. PDFs should be useful in local wind quality assessment, comparison of wind products, data assimilation, development of blended wind products, and air-sea flux

calculations. Furthermore, the observed $P(\delta\mathbf{u})$ can be used to estimate the parameters in stochastic climate models. For example, Sura (2003) developed an empirical stochastic model of midlatitude sea surface winds whose parameters were estimated from $P(\delta\mathbf{u})$ calculated from blended QuikSCAT and NCEP winds. The empirical stochastic modelling approach should be revisited using the ASCAT and new QuikSCAT products.

To help generate ideas and facilitate modeling efforts by the user community, it is recommended that a web-based datamining application should be developed to enable the community to request PDFs for user specified regions and time periods.

References

- Antonia, R. A., M. OuldRouis, F. Anselmet, and Y. Zhu (1997), Analogy between predictions of Kolmogorov and Yaglom, *J. Fluid Mech.*, *332*, 395–409.
- Boffetta, G., and R. E. Ecke (2012), Two-Dimensional Turbulence, *Annu. Rev. Fluid Mech.*, *44*, 427–451, doi:10.1146/annurev-fluid-120710-101240.
- Charney, J. G. (1971), Geostrophic turbulence, *J. Atmos. Sci.*, *28*, 1087–1095.
- Chelton, D. B., M. G. Schlax, M. H. Freilich, and R. F. Milliff (2004), Satellite Measurements Reveal Persistent Small-Scale Features in Ocean Winds, *Science*, *303*(5660), 978–983, doi:10.1126/science.1091901.
- Cho, J. Y. N., and E. Lindborg (2001), Horizontal velocity structure functions in the upper troposphere and lower stratosphere, 1. Observations, *J. Geophys. Res.*, *106* (D10), 10,223–10,232, doi:10.1029/2000JD900814.
- Dewan, E. (1997), Saturated-cascade similitude theory of gravity wave spectra, *J. Geophys. Res. - Atmos.*, *102*, 29,799–29,817.
- Dewan, E. M. (1979), Stratospheric wave spectra resembling turbulence, *Science*, *204*, 832.
- Figa-Saldaña, J., J. Wilson, E. Attema, R. Gelsthorpe, M. Drinkwater, and A. Stoffelen (2002), The advanced scatterometer (ASCAT) on the meteorological operational (MetOp) platform: A follow on for the European wind scatterometers, *Can. J. Remote Sens.*, *28*, 404–412, doi:10.5589/m02-035.
- Fore, A., B. Stiles, A. Chau, B. Williams, R. S. Dunbar, and E. Rodriguez (2012), Point-wise Wind Retrieval and Ambiguity Removal Improvements for the QuikSCAT Climatological Data Set.
- Freilich, M. H., and D. B. Chelton (1986), Wavenumber spectra of Pacific winds measured by the Seasat scatterometer, *J. Phys. Oceanogr.*, *16*, 751–757.
- Frisch, U. (1995), *Turbulence: The legacy of A. N. Kolmogorov*, 296 pp., Cambridge University Press.
- Gage, K. S. (1979), Evidence for a $k^{-5/3}$ law inertial range in mesoscale two-dimensional turbulence, *J. Atmos. Sci.*, *36*, 1950–1954.

- Hanley, K. E., S. E. Belcher, and P. P. Sullivan (2010), A Global Climatology of Wind-Wave Interaction, *J. Phys. Oceanogr.*, *40*(6), 1263–1282, doi:10.1175/2010JPO4377.1.
- Hoffman, R. N., and S. M. Leidner (2005), An introduction to the near-real-time QuikSCAT data, *Wea. Forecasting*, *20*, 476–493, doi:10.1175/WAF841.1.
- Houze, R. A. (2004), Mesoscale convective systems, *Rev. Geophys.*, *42*, RG4003, doi:10.1029/2004RG000150.
- Kármán, T. v., and L. Howarth (1938), On the statistical theory of isotropic turbulence, *Proc. R. Soc. Lond. A*, *164*, 192–215, doi:10.1098/rspa.1938.0013.
- King, G. P., J. Vogelzang, and A. Stoffelen (2012), Second-order structure function analysis of scatterometer winds over the Tropical Pacific: Part 1. Spectra and Structure Functions, *Tech. rep.*, NWPSAF-KN-VS-008, EUMETSAT.
- King, G. P., J. Vogelzang, and A. Stoffelen (2013), Second-order structure function analysis of scatterometer winds over the tropical Pacific: Part 2. Rainy and dry regions, *Tech. rep.*, NWPSAF-KN-VS-012, EUMETSAT.
- KNMI (2011), *ASCAT Wind Product User Manual*.
- Kolmogorov, A. N. (1941), Dissipation of energy in locally isotropic turbulence, *Dokl. Akad. Nauk. SSSR*, *32*, 19–21.
- Lander, M. A. (1996), Specific Tropical Cyclone Track Types and Unusual Tropical Cyclone Motions Associated with a Reverse-Oriented Monsoon Trough in the Western North Pacific, *Wea. Forecasting*, *11*(2), 170–186, doi:10.1175/1520-0434(1996)011<0170:STCTTA>2.0.CO;2.
- Laupattarakasem, P., W. Jones, K. Ahmad, and S. Veleva (2005), Calibration/validation of the SeaWinds radiometer rain rate algorithm, in *OCEANS, 2005. Proceedings of MTS/IEEE*, vol. 3, pp. 2601–2604, doi:10.1109/OCEANS.2005.1640163.
- Lilly, D. K. (1983), Stratified turbulence and the mesoscale variability of the atmosphere, *J. Atmos. Sci.*, *40*, 749–761.
- Lilly, D. K. (1989), Two-dimensional turbulence generated by energy sources at two scales, *J. Atmos. Sci.*, *46*, 2026–2030.
- Lindborg, E. (1996), A note on Kolmogorov’s third-order structure-function law, the local isotropy hypothesis and the pressure-velocity correlation, *J. Fluid Mech.*, *326*, 343–356.
- Lindborg, E. (1999), Can the atmospheric kinetic energy spectrum be explained by two-dimensional turbulence?, *J. Fluid Mech.*, *388*, 259–288.
- Lindborg, E. (2007), Horizontal Wavenumber Spectra of Vertical Vorticity and Horizontal Divergence in the Upper Troposphere and Lower Stratosphere, *J. Atmos. Sci.*, *64*(3), 1017–1025, doi:10.1175/JAS3864.1.

- Lindborg, E., and J. Y. N. Cho (2001), Horizontal velocity structure functions in the upper troposphere and lower stratosphere, 2. Theoretical considerations, *J. Geophys. Res.*, *106* (D10), 10,233–10,241, doi:10.1029/2000JD900815.
- Liu, W. T., and X. Xie (2002), Double intertropical convergence zones — a new look using scatterometer, *Geophys. Res. Lett.*, *29*, 2072, doi:10.1029/2002GL015431.
- Mahrt, L., and N. Gamage (1987), Observations of Turbulence in Stratified Flow, *J. Atmos. Sci.*, *44* (7), 1106–1121, doi:10.1175/1520-0469(1987)044<1106:OOTISF>2.0.CO;2.
- Masunaga, H., and T. S. L’Ecuyer (2010), The southeast Pacific warm band and double ITCZ, *J. Climate*, *23*, 1189–1208, doi:10.1175/2009JCLI3124.1.
- Mitchell, T. P., and J. M. Wallace (1992), The annual cycle in equatorial convection and sea surface temperature, *J. Climate*, *5*, 1140–1156.
- Nastrom, G. D., and K. S. Gage (1985), A Climatology of Atmospheric Wavenumber Spectra of Wind and Temperature Observed by Commercial Aircraft, *J. Atmos. Sci.*, *42*, 950–960.
- Nastrom, G. D., K. S. Gage, and W. H. Jasperson (1984), Kinetic energy spectrum of large-and mesoscale atmospheric processes, *Nature*, *310*, 36–38, doi:10.1038/310036a0.
- Patoux, J., and R. A. Brown (2001), Spectral analysis of QuikSCAT surface winds and two-dimensional turbulence, *J. Geophys. Res.*, *106* (D20), 23,995–24,005, doi:10.1029/2000JD000027.
- Patoux, J., and R. Foster (2012), Cross-Validation of Scatterometer Measurements via Sea-Level Pressure Retrieval, *IEEE Trans. Geosci. Remote Sens.*, *50*(7), 2507–2517, doi:10.1109/TGRS.2011.2172620.
- Patoux, J., R. C. Foster, and R. A. Brown (2010), A method for including mesoscale and synoptic-scale information in scatterometer wind retrievals, *J. Geophys. Res.*, *115*(D11), D11,105, doi:10.1029/2009JD013193.
- Portabella, M., and A. Stoffelen (2002), A comparison of KNMI Quality Control and JPL Rain Flag for SeaWinds, *Can. J. Remote Sens.*, *28*, 424–430.
- Portabella, M., A. Stoffelen, W. Lin, A. Turiel, A. Verhoef, J. Verspeek, and J. Ballabrera-Poy (2012), Rain effects on ASCAT retrieved winds: Towards an improved quality control, *IEEE Trans. Geosci. Remote Sens.*, *50*, 2495–2506, doi:10.1109/TGRS.2012.2185933.
- Risien, C. M., and D. B. Chelton (2008), A Global Climatology of Surface Wind and Wind Stress Fields from Eight Years of QuikSCAT Scatterometer Data, *J. Phys. Oceanogr.*, *38*, 237–2413, doi:10.1175/2008JPO3881.1.
- Rodriguez, E., and A. Chau (2011), Improved wind directions, divergence, vorticity and their spectra for the QuikSCAT scatterometer, *J. Geophys. Res.*

- Small, R. J., S. deSzoeko, S. Xie, L. O'Neill, H. Seo, Q. Song, P. Cornillon, M. Spall, and S. Minobe (2008), Air-sea interaction over ocean fronts and eddies, *Dyn. Atmos. Oceans*, *45*, 274–319.
- Stiles, B., B. Pollard, and R. Dunbar (2002), Direction interval retrieval with thresholded nudging: A method for improving the accuracy of QuikSCAT winds, *IEEE Trans. Geosci. Remote Sens.*, *40*, 79–89.
- Sura, P. (2003), Stochastic Analysis of Southern and Pacific Ocean Sea Surface Winds, *J. Atmos. Sci.*, *60*(4), 654–666, doi:10.1175/1520-0469(2003)060<0654:SAOSAP>2.0.CO;2.
- Tsai, W.-T., M. Spencer, C. Wu, C. Winn, and K. Kellogg (2000), SeaWinds on QuikSCAT: sensor description and mission overview, in *Geoscience and Remote Sensing Symposium, 2000. Proceedings. IGARSS 2000. IEEE 2000 International*, vol. 3, pp. 1021–1023 vol.3, doi:10.1109/IGARSS.2000.858008.
- Van Zandt, T. E. (1982), A universal spectrum of buoyancy waves in the atmosphere, *Geophys. Res. Lett.*, *9*, 575–578.
- Vogelzang, J., A. Stoffelen, A. Verhoef, J. de Vries, and H. Bonekamp (2009), Validation of two-dimensional variational ambiguity removal on SeaWinds scatterometer data, *J. Atmos. Oceanic Technol.*, *26*, 1229–1245, doi:10.1175/2008JTECHA1232.1.
- Wikle, C. K., R. F. Milliff, and W. G. Large (1999), Surface wind variability on spatial scales from 1 to 1000 km observed during TOGA COARE, *J. Atmos. Sci.*, *56*, 2222–2231.
- Wyrтки, K. (1989), Some thoughts about the west Pacific warm pool, in *Proceedings of the Western Pacific International Meeting and Workshop on TOGA COARE*, edited by J. Picaut, R. Lucas, and T. Delcroix, pp. 99–109, New Caledonia, ORSTUM, Centre de Nouma.
- Xu, Y., L.-L. Fu, and R. Tulloch (2011), The global characteristics of the wavenumber spectrum of ocean surface wind, *J. Phys. Oceanogr.*, *41*, 1576–1582, doi:10.1175/JPO-D-11-059.1.
- Zhu, B., and B. Wang (1993), The 30–60-day convection seesaw between the Tropical Indian and Western Pacific Oceans, *J. Atmos. Sci.*, *50*, 184–199, doi:10.1175/1520-0469(1993)050<0184:TDCSBT>2.0.CO;2.